



UNIVERSITY **POLITEHNICA** OF BUCHAREST

Doctoral School of Electrical Engineering

PHD Thesis

Energy conversion models in low power applications

– Summary –

Author: Eng. Yelda VELI

Scientific coordinator: Prof.PhD.Eng. Alexandru Mihail MOREGA

Bucharest 2021

Content

INTRODUCTION	5
CHAPTER 1 ENERGY HARVESTING FOR LOW POWER APPLICATIONS	6
1.1. ENERGY HARVESTING SYSTEMS	6
1.2 PRINCIPLES AND METHODS FOR HARVESTING ENVIRONMENTAL ENERGY	6
1.2.1. <i>Solar energy</i>	6
1.2.2. <i>Mechanical energy</i>	6
1.2.3. <i>Thermal energy</i>	6
1.2.4. <i>Other sources of energy</i>	6
CHAPTER 2 CONVERTERS FOR HARVESTING MECHANICAL ENERGY	7
2.1 PIEZOELECTRIC BIOMECHANICAL ENERGY HARVESTING DEVICE	7
2.1.1. <i>Computational domain</i>	7
2.1.2. <i>Mathematical model</i>	7
2.1.3. <i>Numerical simulation results</i>	8
2.2. MAGNETOSTRICTIV ACTUATOR	8
2.2.1. <i>Physical, computational domain</i>	8
2.2.2. <i>Mathematical model of the MSA</i>	9
2.2.3. <i>Numerical simulation results</i>	11
2.2.4 <i>Mechanical-electrical spectral analysis</i>	12
2.2.5. <i>Conclusions</i>	14
2.3 EH DEVICE BY ARTERIAL WALL DEFORMATION	14
2.3.1. <i>Computational domain</i>	14
2.3.2. <i>Mathematical model</i>	14
2.3.3. <i>Numerical simulation results</i>	15
2.4 CONCLUSIONS	16
CHAPTER 3. CONDITIONING OF THE HARVESTED ENERGY	16
3.1 INTRODUCTION	16
<i>The conditioning stage adjusts the impedances by reducing voltage and current variations.</i>	16
3.1.1 <i>Electrostatic switching dc – dc converters</i>	16
3.1.2 <i>Magnetic switching dc – dc converters.</i>	16
3.2 FLYBACK CONVERTERS	16
3.2.1 <i>Construction and functioning.</i>	16
3.2.2 <i>Flyback converter inductors</i>	17
3.2.3 <i>Constructive design</i>	17
3.3 A SIMPLIFIED MODEL FOR AN INDUCTOR (TRANSFORMER) WITH SPIRAL PLANAR WINDINGS	17
3.3.1 <i>Physical model of the electromagnetic field in the FB inductor</i>	17
3.3.2 <i>Determination of steady state circuit parameters</i>	18
3.3.3 <i>Numerical results of the simplified stationary transformer</i>	19
3.3.4 <i>Numerical results of the transformer, powered by a PWM voltage source at 1 kHz.</i>	19
3.4 THE MODEL OF A FB MINIATURE, PLANAR, SIMPLIFIED INDUCTOR WITH MNF– CONCEPTUAL SIMPLIFIED MODEL	20
3.4.1 <i>Computational domain</i>	20
3.4.2 <i>Load circuit design for different constructive alternatives</i>	21
3.4.3 <i>Numerical simulation results for a miniature, simplified FBT in quasi-stationary mode, powered by a PWM voltage source at 10 kHz.</i>	22
3.5 GALVANIC SEPARATION TRANSFORMER	24
3.5.1 <i>Galvanically isolated transformer in energy harvesting systems</i>	24
3.5.2 <i>Computational domain</i>	24

3.5.4 Numerical simulation results	25
3.6 CONCLUSIONS	25
CHAPTER 4 STORAGE OF HARVESTED ENERGY	26
4.1 INTRODUCTION	26
4.2 ENERGY STORING DEVICES	26
4.2.1 Batteries	26
4.2.2 Supercapacitors.....	26
4.2.3 Other energy storage devices	26
4.3 COMPACT, INTERDIGITATED SUPERCAPACITOR SYSTEMS.....	26
4.3.1 Supercapacitors with carbon nanotubes	26
4.3.2 Computational domain.....	26
4.3.3 Numerical simulation results	27
4.4 CONCLUSIONS	28
CHAPTER 5 WIRELESS SENSOR NETWORKS	28
5.1 INTRODUCTION	28
5.2 WIRELESS SENSOR NODES	29
5.2.1 Main components of wireless sensor nodes.....	29
5.2.2 Wireless sensor nodes characteristics	29
5.2.3 Network topologies	29
5.3 WIRELESS SENSOR NETWORK SIMULATION	30
5.3.1 Network configuration	30
5.3.3 Conclusions	31
GENERAL CONCLUSIONS, CONTRIBUTIONS AND FUTURE PERSPECTIVES ..	32
C1. GENERAL CONCLUSIONS	32
C2. ORIGINAL CONTRIBUTIONS	33
C3. FUTURE PERSPECTIVES	33
ANEXE	34
BIBLIOGRAFIE	35

INTRODUCTION

The Phd thesis is structured in five chapters to which are added the introduction and personal contributions, the development perspectives, respectively. The thesis follows the structure of a general energy harvesting system, from the primary converter, to the conditioning stage of the harvested energy, respectively the storage stage, to the supply of the final consumers. The structure of the energy harvesting system is repeated at the beginning of each chapter.

Chapter 1, "Energy harvesting for low power applications", is a state-of-the art on the sources, methods and materials used in harvesting systems.

Chapter 2, "Converters for harvesting mechanical energy" examines three harvesting devices. The first device uses piezoelectric materials. Two constructive models are analyzed. The second analyzed device is a magnetostrictive actuator (MSA) for which there is a need of a spectral analysis. The optimal level of the mechanical spring prestress is established. The operation at excitation in current and in *PWM* voltage is compared. The last device uses the deformation movement of the arterial walls to extract electrical voltage.

Chapter 3, "Conditioning of harvested energy" is dedicated to the energy conditioning stage. Some converters and inductors used in this step are presented, as well as the principle and modes of operation of the flyback converter. Models of different complexities are analyzed. The first model is an inductor (transformer) supplied from a direct current source, respectively a *PWM* voltage source, for which different regimes are analyzed: open-circuit, short circuit and load, and concentrated circuit parameters are calculated. We then analyze a flyback inductor for which we have two constructive models: with air and non-magnetic media, and with magnetic nanofluid (MNF 500), respectively. For these two alternatives, the optimal size of the air gap is established, for which we get the largest amount of stored magnetic energy. The load circuit is dimensioned, and a thermal study is conducted. The last analyzed inductor model has spiral windings, not cylinders (simplified variant). Last part is concerned with the operation of a transformer with galvanic insulation, for which a parametric study is performed. Different dimensions of the space between the windings are modelled, and the positioning of the magnetic screen is done accordingly. The circuit parameters values are computed.

Chapter 4, "Storage of harvested energy" is a state-of-the-art study of the available energy storage devices. The alternatives that we have available at the moment is outlined. In the last part of the chapter a supercapacitor with carbon nanotubes is studied. The analysis is a documentary one, the model is from the literature and involves the structural and constructive optimization of the elementary cell of the supercapacitor for which various higher order assemblies are subsequently made.

Chapter five, "Wireless sensor networks" aims to analyze the last stage of an EH system, namely the end consumers represented by the nodes of a wireless sensor network. A WSN network, with nodes randomly placed on a given surface of a given size is simulated. A multi-hop routing protocol is analyzed. For this way of communication, two cases are considered, a 30 nodes network, and a 50 nodes network, respectively.

CHAPTER 1 ENERGY HARVESTING FOR LOW POWER APPLICATIONS

1.1. ENERGY HARVESTING SYSTEMS

The harvesting unit is represented by the primary converter.

The storing unit is optional and comprised of batteries and/or supercapacitors.

The energy conversion unit is composed of different converters, transformers and inductors with the role of adapting the energy collected.

The load unit is made of different sensors, microcontrollers etc.

1.2 PRINCIPLES AND METHODS FOR HARVESTING ENVIRONMENTAL ENERGY

1.2.1. Solar energy

The efficiency of photovoltaic conversion is also affected by the reflection of incident sunlight in the cell, when electrons recombine with the gaps.

The Construction Law (CL) dictates the evolution of flow in systems over time, reaching superior configurations to provide easier access to the currents flowing through them [1-2]. LC represents an optimization criterion of FV cells.

The maximum power point - MPP - indicates the point on the current-voltage characteristic graph, determined by the intersection of the values of the short-circuit current with the open-circuit voltage, when the value of the product between them is maximum [3,4].

The tracking system optimizes the position of the PV cell relative to the MPP.

1.2.2. Mechanical energy

Different converters are used to harvest energy from different mechanical energy sources whose power must be known in advance. *Mechanical electromagnetic (inductive) converters* use the law of electromagnetic induction for mechano-electrical conversion. *Electrostatic mechanical energy converters* are the second category of devices used in the conversion of mechanical energy. *Piezoelectric converters* use the direct piezoelectric properties of piezoelectric materials. There are two operating modes, d_{33} and mode 31, d_{31} , respectively. *Magnetostrictive generators* use a deformation field to provide a magnetic field.

1.2.3. Thermal energy

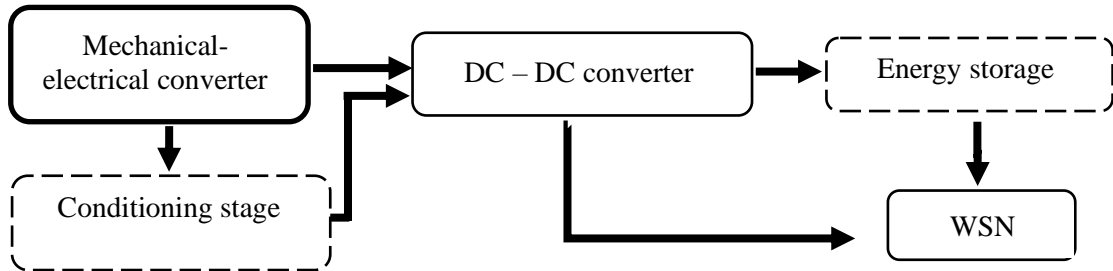
Thermoelectric effects (Peltier, Seebeck, Thomson) are used for thermoelectric conversion.

1.2.4. Other sources of energy

The energy provided by radio frequency (RF) waves refers to the energy provided by various electronic devices. Harvesting from acoustic energy sources is another efficient method of supplying low power consumers [5-8].

CHAPTER 2 CONVERTERS FOR HARVESTING MECHANICAL ENERGY

Figure 2.1 shows the diagram of a mechanical EH system. With dotted lines optional blocks are represented. The primary mechanical-electrical converters are analyzed.



2.1. Block diagram of a mechanical energy harvesting system.

Three conversion devices, that use different principles and phenomena are presented.

2.1 PIEZOELECTRIC BIOMECHANICAL ENERGY HARVESTING DEVICE

2.1.1. Computational domain

Figure 2.2 shows the 3D computational domain and the mesh of the adapted device, with a single, and with two limiting blades, respectively.

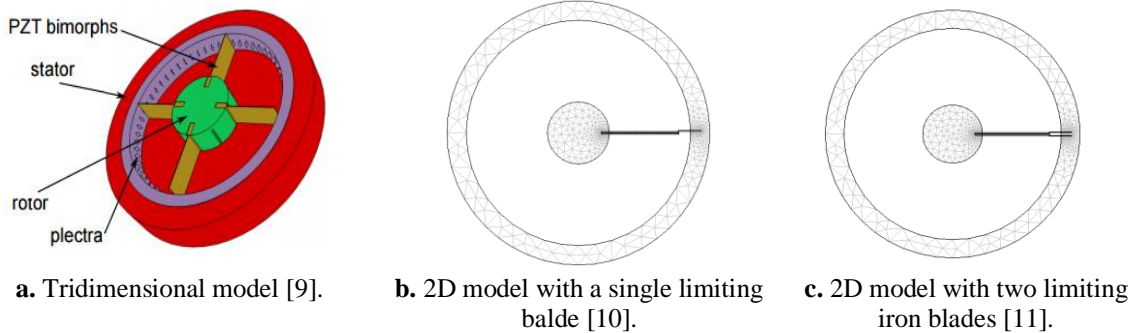


Fig. 2.2 3D computational domain and simplified 2D discretization network with one and two limiting blades, respectively.

The device consists of a stator and a rotor that have at their proximal ends some bimorphic PZT material blades integrated between two layers of foam between two other layers of aluminum.

2.1.2. Mathematical model

The relation between the piezoelectric coefficients is given by [9]:

$$G = dK\varepsilon_0, \quad (2.1)$$

where d [m/V] is the piezoelectric coefficient, K is the coupling factor and G [Vm/N] is the open circuit coefficient. The mathematical model which describes the electric and structural field coupling is given by:

$$\begin{aligned}\mathbf{T} &= s_E \cdot \mathbf{T} - \mathbf{d}^t \cdot \mathbf{E} \\ \mathbf{D} &= \mathbf{d} \cdot \mathbf{S} + \varepsilon_0 \varepsilon_r \cdot \mathbf{E}\end{aligned}\quad (2.2)$$

where \mathbf{T} is the strain, \mathbf{S} is the stress, s_E [Pa^{-1}], and \mathbf{d} [V^{-1}], respectively is the compliance and coupling matrix, respectively, $(\mathbf{d})^t$ is the transposition operator, \mathbf{E} [V/m] is the electric field strength, \mathbf{D} [C/m^2] is the electric flux density, ε_0 and ε_r are the electrical permittivity of free space and the relative electric permittivity, respectively.

2.1.3. Numerical simulation results

The maximum deformations for both constructive cases for rotational angles of $\alpha = 0^\circ \dots 3,1^\circ$, and $\alpha = 0^\circ \dots 2^\circ$, respectively are presented in Fig. 2.3, amplified two times.

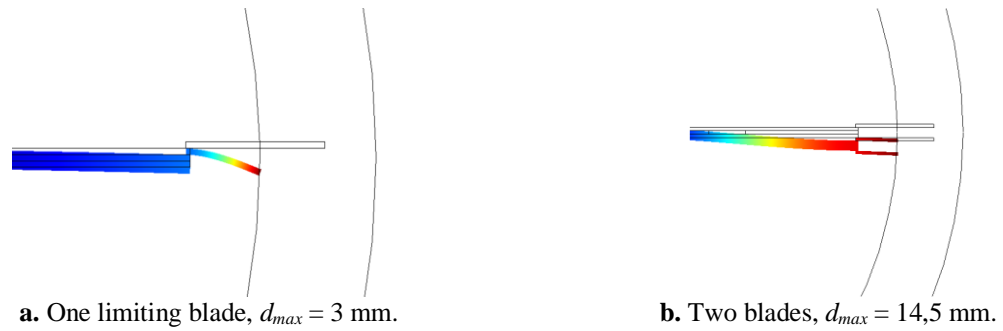


Fig. 2.3. Deforming field of the PZT and limiting blades for both models, amplified two times.

The electric potential for both models is presented in Fig. 2.4.

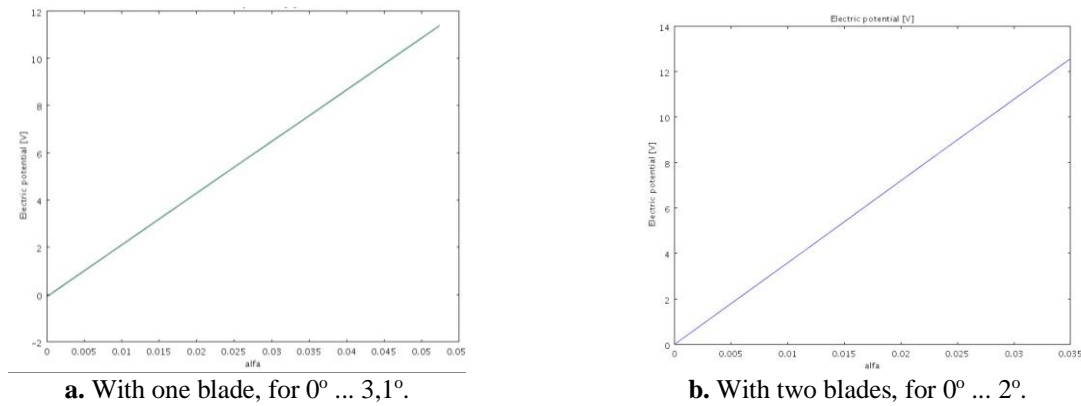


Fig. 2.4. Piezoelectric voltage for both models, with one and two limiting blades..

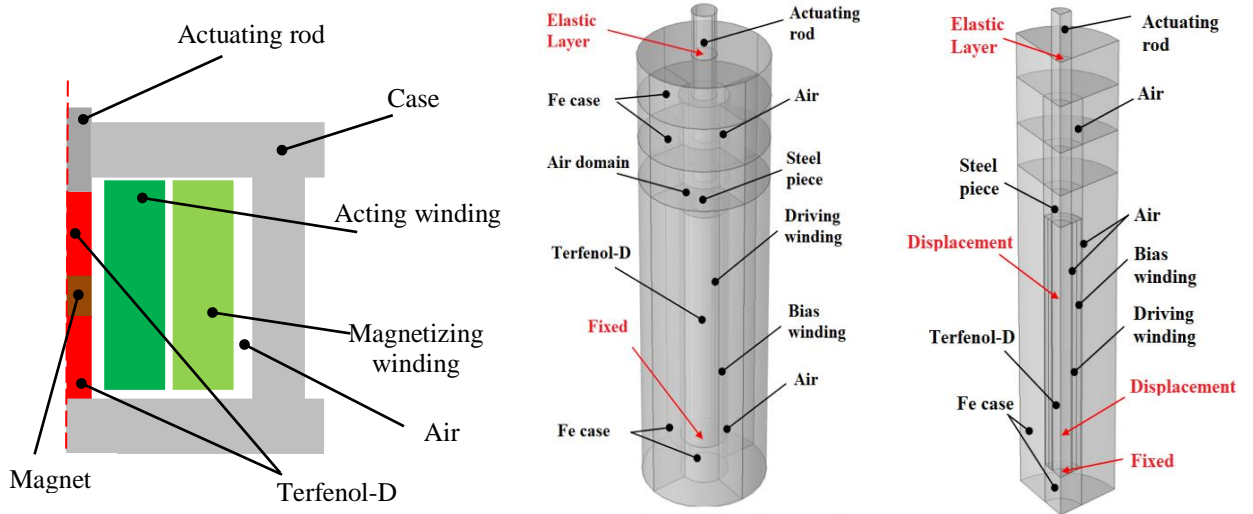
The portable piezoelectric device is versatile, flexible and scalable. It can be used on different joints and can be adapted by incorporating several PZT blades.

2.2. MAGNETOSTRICTIV ACTUATOR

Magnetostrictive actuators (MSA) use a magnetostrictive medium (MS) that can be deformed by a magnetic field provided by magnets and / or windings.

2.2.1. Physical, computational domain

In Fig. 2.5, a is the 2D computational domain with axial symmetry used only in *PWM* current supply, followed by the 3D domains that allowed the *PWM* voltage excitation of the windings, used in solving various field problems.



a. 2D with axial symmetry domain – after [12].

b. 3D domain used in structural field [13].

c. a quarter of the domain, used in electromagnetic field [13].

Fig. 2.5. Computational domains for 2D with axial symmetry model and 3D, respectively.

For the 2D model we analyze different structures of MMS for which a constructive optimization is performed [12]. The results are compared with those obtained for *PWM* voltage excitation, where the premagnetization field is created only by the magnetizing winding (bias).

2.2.2. Mathematical model of the MSA

For Fig. 25,a the mathematical model described by the magnetic potential due to the azimuthal component and the supply amperturns is:

$$\sigma \frac{\partial \mathbf{A}}{\partial t} + \nabla \times \mathbf{H} = 0, \quad (2.3)$$

For the MS material:

$$\sigma \frac{\partial \mathbf{A}}{\partial t} + \nabla \times (\mu_0^{-1} \mu_r^{-1} \nabla \times \mathbf{A}) = \mathbf{J}_\varphi^e, \quad (2.4)$$

where \mathbf{J}_φ^e [A/m²] is the electric current density, azimuthal component, \mathbf{H} [A/m] is the magnetic field strength and $\mathbf{A} = A_\varphi \mathbf{e}_\varphi$ [T·m] is the magnetic vector potential, azimuthal component.

The MS coefficient expresses in linear limits the strain and magnetization state [12]:

$$\lambda_{r,z} = \frac{3}{2} \lambda_S \left(\alpha_{r,z}^2 - \frac{1}{3} \right) = \frac{3}{2} \lambda_S \left[\left(\frac{M_{r,z}}{M_S} \right)^2 - \frac{1}{3} \right], \quad (2.5)$$

where $\lambda_{r,z}$ is the MS coefficient in *r* and *z* directions, which depends on the value of the MS constant, λ_S .

The electromagnetic field is described by the electromagnetic induction, and conduction law, respectively, and by magnetic and electric circuit law [12-16]:

$$\nabla \times \mathbf{E} = -\frac{\partial \mathbf{B}}{\partial t}, \quad \nabla \cdot \mathbf{B} = 0, \quad \nabla \times \mathbf{H} = \mathbf{J}, \quad \mathbf{J} = \sigma \mathbf{E}. \quad (2.6)$$

Here, \mathbf{E} [V/m] is the electric field strength, \mathbf{B} [T] is the magnetic flux density, σ [S/m] is the electrical conductivity, and, μ [H/m] is the magnetic permeability. The magnetic field of the displacement current density is neglected here.

The constitutive law for MMS is [13]:

$$\mathbf{B} = \mu_0 [\mathbf{H} + \mathbf{M}(\mathbf{H}, S_m) + \mathbf{M}_r], \quad (2.7)$$

where \mathbf{M} [A/m] is the temporarily magnetization deformarea mecanică, S_m , and \mathbf{M}_r [A/m] is the remanent magnetization.

The nonlinear dependency of MS coefficient with respect of the magnetic field and strain is [13]

$$\lambda = \frac{3}{2} \lambda_s \left(\frac{M}{M_s} \right)^2, \quad (2.8)$$

$\lambda_s = 0.0012$ is the MS constant [2], and \mathbf{M}_s [A/m] is the saturation magnetization. The magnetic core, from soft iron, is magnetically isolated. The linear constitutive laws that describe the coupling inside MMS, regardless of the powering scheme, is given by [13]:

$$\begin{aligned} S &= \eta_H T + dH \\ B &= dT + \mu_T H \end{aligned} \quad (2.9)$$

where S [1] is the strain, T [N/m²] is the stress, $\eta_H = \partial S / \partial H$ is the compliance at constant magnetic field, d [m/A] is the piezomagnetic constant and μ_T [H/m] is the magnetic permeability at constant strain. The strain-stress relation because of prestress is described by the generalized Hooke`s law [13,17-18]:

$$T = C(S - S_i) + T_i, \quad (2.10)$$

where C [N/m] is the stiffness and $(\cdot)_i$ indicates the initial state. The uniaxial assumption links the MSC shape change to stress $S = \partial w / \partial z$, which is subject of the strain gradient $\partial T / \partial z = \rho \partial^2 w / \partial z^2$, where $w = w(z(t))$ is the position and ρ [kg/m³] is the mass density. Using (2.7) and (2.10) and the above relations, the mathematical model for MSC is [19-24]

$$\begin{aligned} -\frac{\rho d^2}{\mu} \frac{\partial^2 H}{\partial t^2} + \mu \sigma \frac{\partial H}{\partial t} &= \nabla^2 H + \frac{d \rho \eta}{\mu} \frac{\partial^2 T}{\partial t^2} - \sigma d \frac{\partial T}{\partial t}, \\ \rho \eta \frac{\partial^2 T}{\partial t^2} &= \frac{\partial^2 T}{\partial z^2} - \rho d \frac{\partial^2 H}{\partial t^2}. \end{aligned} \quad (2.11)$$

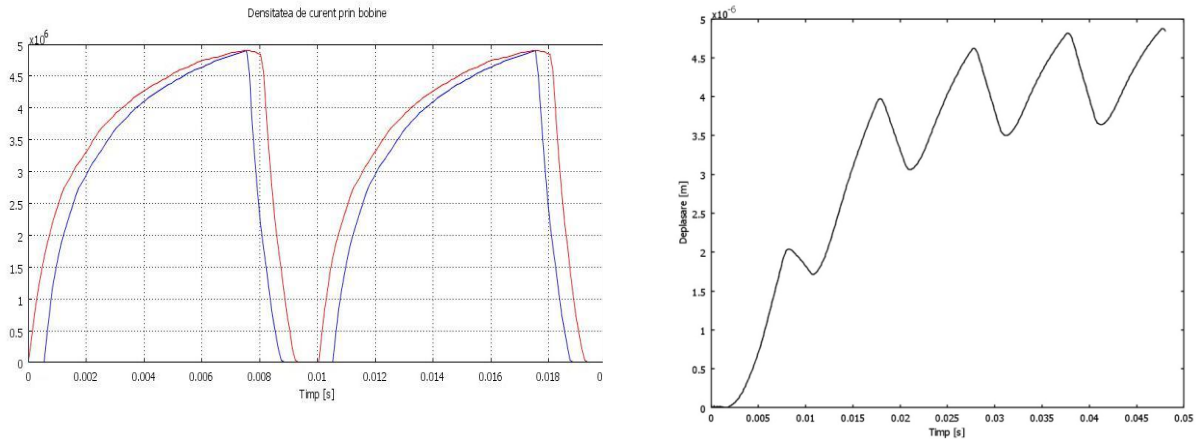
The coupling (2.11) is applied only to MSC. For all other domains (2.10) becomes:

$$\mu \sigma \frac{\partial \mathbf{H}}{\partial t} = \nabla^2 \mathbf{H}. \quad (2.12)$$

2.2.3. Numerical simulation results

PWM current excitation (model with one magnet in the MSC)

Figure 2.6 presents the excitation current for driving, and bias coils, respectively, for $f_{PWM} = 100$ Hz (Fig. 2.5,a), and also the displacement of the actuating rod.



a. electric current density coil excitation.

b. the displacement of the actuating rod.

Fig. 2.6. The exciting current at $f_{PWM} = 100$ Hz and $k_{act} = 70$ %, and the displacement of the actuating rod without prestress[12].

Different duty cycles were used, $k_{act} = 70\%$ and $k_{bias} = 80\%$, respectively. For this model a structural optimization is conducted by varying the height and then the number of permanent magnets from MSC structure, without changing the volume.

PWM voltage excitation (model without magnet in MSC structure)

The mathematical model from (2.7) – (2.13) was solved for the computational domain from Fig. 2.11,c. The excitation currents were deducted from the PWM voltage supply model. Reduced displacements and longer stabilization time is depicted for PWM current excitation.

The friction effect on the output connector – slip fit bearing

The displacement of the actuating rod, with friction, $c_f = 0.01$ [17,25] presents lower values and a slight delay compared with the model without friction.

Mechanical Prestress

The MSC deformation is depicted in Fig. 2.7, amplified by 5 times, for two moments which corresponds with the extreme positions of the rod for $F_{PS} = 500$ N/m, without friction.

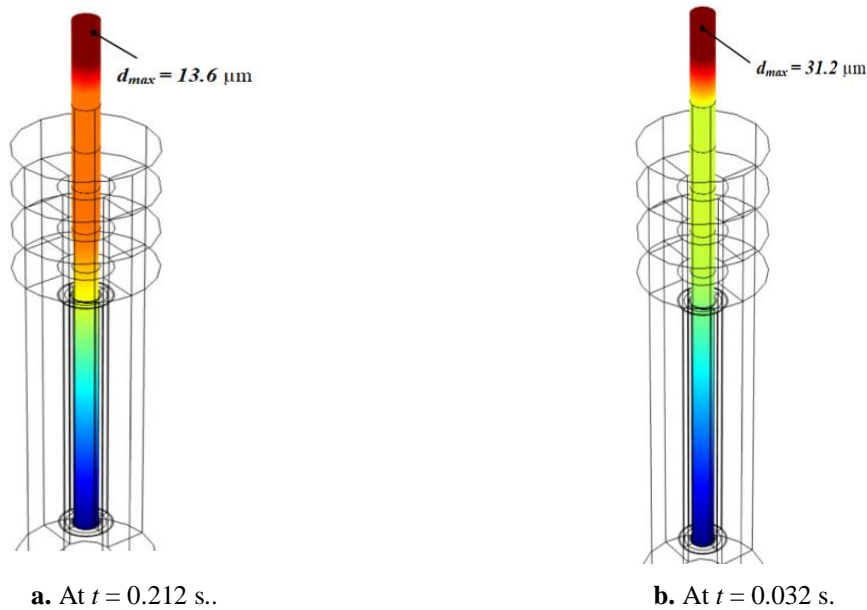


Fig. 2.7. The displacement of the actuating rod for two different times. Friction is neglected.

Figure 2.8 depicts the displacement of the rod for different prestress levels, F_{PS} .

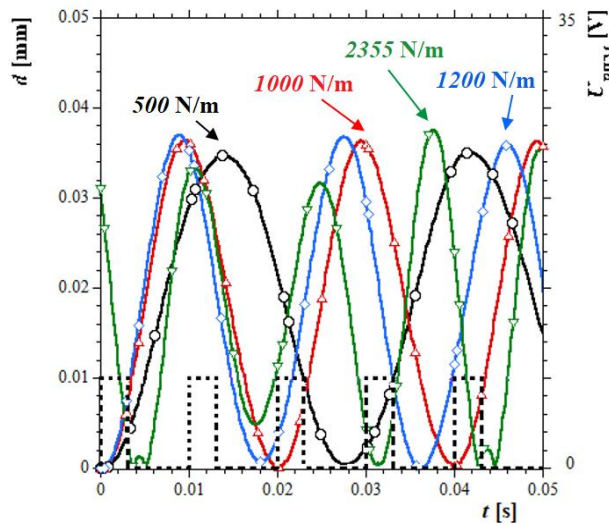


Fig. 2.8. The displacement of the actuating rod with increase prestress level, F_{PS} .

There is a relation between the mechanical eigenfrequencies and the electromagnetic properties and also the PWM frequency spectrum.

2.2.4 Mechanical-electrical spectral analysis

The frequency spectrum for voltage excitation at 30 V, $f_{PWM} = 100$ Hz, $k = 30\%$ is in Fig. 2.9. The most significant frequency is $f_e = 150$ Hz, electrical frequency which, together with $f_{PWM} = 100$ Hz, will be compared to the mechanical eigenfrequencies, f_m .

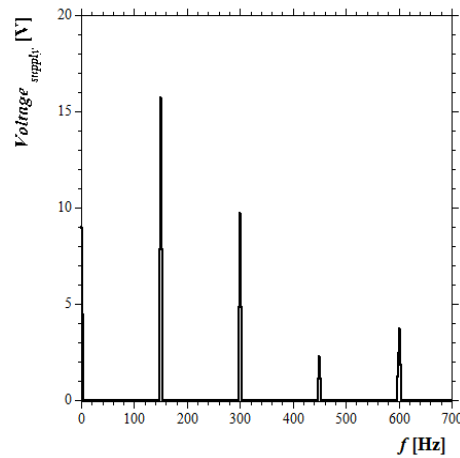


Fig. 2.9. The frequency components amplitude for PWM voltage supply, at 30 V, $f_{PWM} = 100$ Hz and with $k = 30$ %.

The natural frequencies show the four most important mechanical frequencies, f_m , found around the frequency, f_e and are included in Table 2.1, accordingly with the F_{PS} value.

Tabel 2.1 Structural eigenfrequencies around $f_e = 150$ Hz ($f_{PWM} = 100$ Hz) for different prestress values, F_{PS} . Friction is neglected.

F_{PS} [N/m]	$f_{m,1}$ [Hz]	$f_{m,2}$ [Hz]	$f_{m,3}$ [Hz]	$f_{m,4}$ [Hz]
500	43.237	70.511	132.51	213.04
750	47.571	85.113	138.23	263.01
1000	49.815	97.583	143.84	293.583
1200	48.986	102.406	158.02	291.437
1500	47.396	119.245	164.24	292.951
2355	47.368	150.001	188.11	290.87

Adjusting the PWM frequency

Tabel 2.2 presents the electrical fundamental frequencies, f_e , and the first most significant displacement frequencies, f_d , at $f_{PWM} = 100$ Hz, 85 Hz and 43 Hz.

Tabel 2.2 The electrical, f_e , and displacement frequencies, f_d , for different f_{PWM} * values.

f_{PWM} [Hz]	f_e [Hz]**	f_d [Hz]*		
		$f_{d,1}$	$f_{d,2}$	$f_{d,3}$
43	68	7.45	9.09	1.63
85	127	5.11	7.06	17.05
100	150	8.36	3.58	20.30

* $k = 30\%$, $F_{PS} = 500$ N/m; ** Values are rounded.

Table 2.2 shows the eigenfrequencies ($f_{m,1} = 43.237$ Hz) close to $f_{PWM} = 43$ Hz and another frequency ($f_{m,2} = 70.511$ Hz) relatively close to its frequency, $f_e = 68$ Hz, but no structural eigenfrequency is not found near $f_{PWM} = 85$ Hz ($f_e = 100$ Hz) or near PWM frequency $f_{PWM} = 100$ Hz ($f_e = 150$ Hz).

2.2.5. Conclusions

The sizing of MSA must take into account f_e and f_m , rather than f_{PWM} .

2.3 EH DEVICE BY ARTERIAL WALL DEFORMATION

2.3.1. Computational domain

An EH device that uses deformation of the arterial wall during a cardiac cycle is analyzed [26-28]. The calculation range is represented in Figs. 2.10.

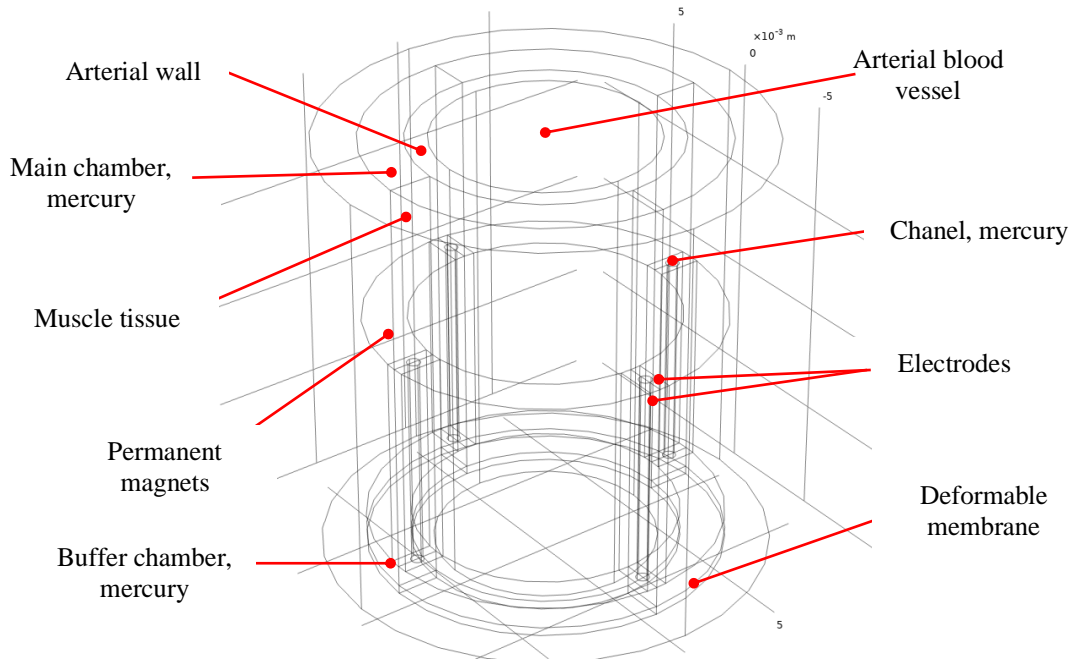


Fig. 2.10. Computational domain and all constituent elements. The dimensions are in meters.

Blood flow causes wall deformation. The fluid is moved in the main chamber (MC) and buffer chamber (BC) through four channels, in a magnetic field. A load resistor is connected to the electrode terminals. A flexible membrane (FM), below the BC, allows the flow in the opposite direction, from the BC to the MC through the 4 channels.

2.3.2. Mathematical model

Blood flow and conductive fluid flow

The Navier-Stokes equations (the momentum conservation law and the law of mass conservation, respectively) fully describe the flow of arterial blood:

$$\rho \frac{\partial \mathbf{u}}{\partial t} + \rho(\mathbf{u} \cdot \nabla) \mathbf{u} = -\nabla p + \eta \nabla^2 \mathbf{u}, \quad (2.13)$$

$$\nabla \cdot \mathbf{u} = 0, \quad (2.14)$$

here \mathbf{u} [m/s] is the blood velocity, ρ [kg/m³] is the mass density, p [Pa] is the pressure, η [Pa·s] represents the dynamic viscosity. For mercury the momentum conservation law is given by:

$$\rho \frac{\partial \mathbf{u}}{\partial t} + \rho(\mathbf{u} \cdot \nabla) \mathbf{u} = -\nabla p + \eta \nabla^2 \mathbf{u} + \mathbf{J} \times \mathbf{B}, \quad (2.15)$$

here \mathbf{J} [A/m²] represents the electrical current density between the electrodes, and \mathbf{B} [T] is the magnetic flux density.

$$\nabla \cdot \mathbf{u} = 0, \quad (2.16)$$

here \mathbf{u} [m/s] is the flow of the mercury.

At the entrance to the blood vessel the systolic pressure is imposed, and at the exit the diastolic one. The walls of the vessel will have a no-slip condition, and a slip condition for the interior boundaries of the chambers.

Deformation field

Hooke's law characterizes mechanical deformation:

$$\boldsymbol{\sigma}_M = \mathbf{E}\boldsymbol{\varepsilon}, \quad (2.17)$$

here $\boldsymbol{\sigma}_M$ represents the strain, \mathbf{E} is the elasticity matrix and $\boldsymbol{\varepsilon}$ is the stress matrix. Fixed boundaries are specified at both ends of the wall and at the interior and exterior membranes so it deforms only on z axis.

Electromagnetic field

The electromagnetic field is given by Faraday's law, the magnetic and electric flux law, the magnetic circuit, the electric conduction, and the electric charge conservation laws:

$$\nabla \times \mathbf{E} = -\frac{\partial \mathbf{B}}{\partial t}, \quad \nabla \cdot \mathbf{B} = 0, \quad \nabla \cdot \mathbf{D} = \rho_v, \quad \nabla \times \mathbf{H} = \mathbf{J}, \quad \mathbf{J} = \sigma \mathbf{E}, \quad \nabla \cdot \mathbf{J} = 0 \quad (2.18)$$

here \mathbf{E} [V/m] is the electric field strength, \mathbf{D} [C/m²] is the electric flux density, ρ_v [C/m³] is the electric charge density, \mathbf{B}_r [T] is the remanent magnetic flux density, \mathbf{H} [A/m] is the magnetic field strength, σ [S/m] is the electrical conductivity.

2.3.3. Numerical simulation results

Figure 2.11 presents the induced open-circuit voltage, and short-circuit current.

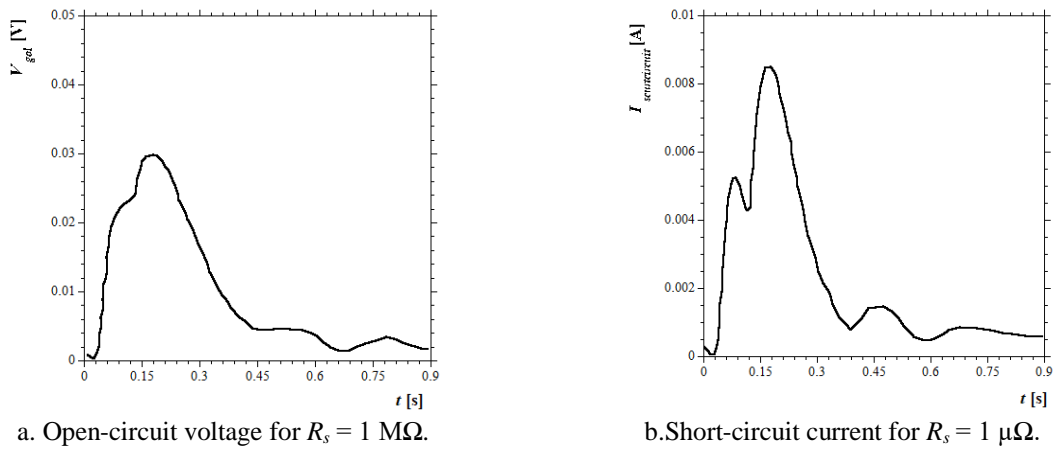


Fig. 2.11. Open-circuit voltage, and short-circuit current at the terminals.

This seems to indicate that the load resistance still has a certain level of power before the start of a new cycle.

2.4 CONCLUSIONS

The piezoelectric device is able to generate much higher voltages by integrating several more blades in its construction.

Increasing the f_{PWM} value is a compromise solution, if the application does not allow adjustment after F_{PS} or f_e and f_m .

The implantable device is able to generate enough energy to power a pacemaker, but if the scalability feature is considered, the power generated can be increased by integrating several flow channels of higher heights.

CHAPTER 3. CONDITIONING OF THE HARVESTED ENERGY

3.1 INTRODUCTION

The conditioning stage adjusts the impedances by reducing voltage and current variations.

3.1.1 Electrostatic switching dc – dc converters

Switching converters have superior performance and are classified, depending on the circuit elements, into electrostatic and magnetic converters [29]. In electrostatic ones, the transfer and conditioning of energy is carried out exclusively by capacitors that are connected to the load in alternating cycles.

3.1.2 Magnetic switching dc – dc converters

In magnetic switching converters the energy is stored through capacitors and its transfer through inductors. Switching losses are minimized. Another alternative is the flyback converter (FBC).

3.2 FLYBACK CONVERTERS

As long as the primary is powered on, the secondary is disconnected, *off*, and magnetic energy is stored through inductances which is then delivered to the load when the secondary switches *on*, and the primary switches *off*. The amount of energy delivered to the load determines how the FBC operates.

3.2.1 Construction and functioning

There are three modes of operation in terms of energy transfer [30-37]:

- Continuous conduction mode (CCM);
- Discontinuous conduction mode (DCM);
- Critical conduction mode or transition conduction mode (TCM).

The magnetic energy stored in DCM is partially delivered to the load, resulting in a rest time between on-off switching which contributes to losses [32]. CCM is characterized by minimal switching losses, almost non-existent rest time.

3.2.2 Flyback converter inductors

Different types of inductors that are part of the FBC are classified according to the number of windings.

3.2.3 Constructive design

Models of different complexities of FBT are presented, gradually, until we reach the unsimplified model for which there is the constructed prototype represented in Fig. 3.1.

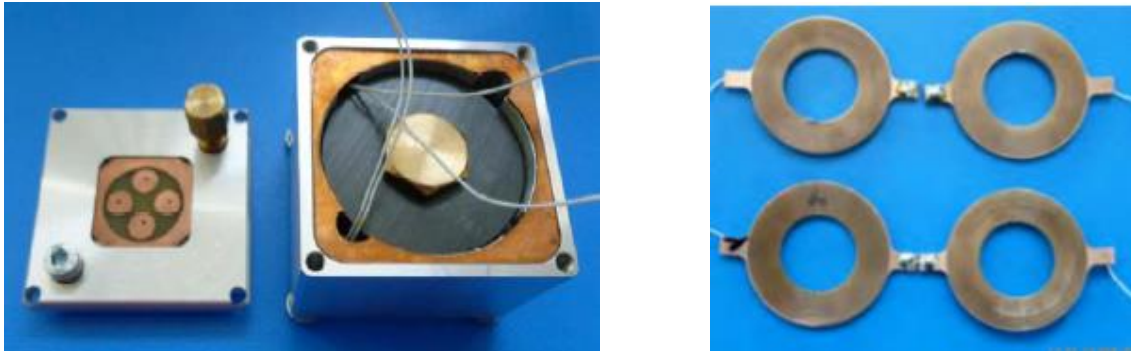


Fig. 3.1. FBT with hybrid core, ferrite and MNF (left) and spiral windings (right) [38].

Constructive models of inductors with non-magnetic media, respectively with magnetic nanofluid media (MNF) will be analyzed.

3.3 A SIMPLIFIED MODEL FOR AN INDUCTOR (TRANSFORMER) WITH SPIRAL PLANAR WINDINGS

The simplified model, shown in Figs. 3.2, is that of a transformer, 1:1, with planar windings, of 30 turns each.

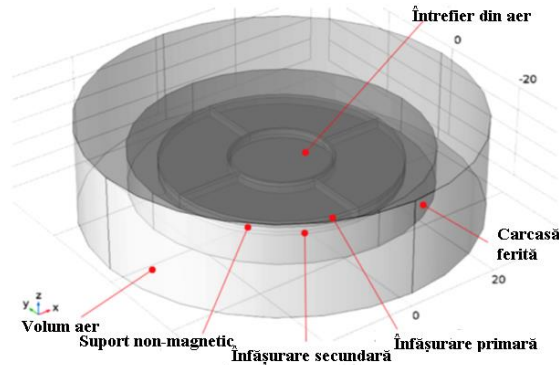


Fig. 3.2. Computational domain of the planar transformer, simplified, with an air gap in the central column of the core. The dimensions are in millimeters. The windings are cylindrical discs.

3.3.1 Physical model of the electromagnetic field in the FB inductor

The electrokinetic problem provides the distribution of electric current density in windings. The electrokinetic model is described by the following relation to partial derivatives:

$$\nabla \cdot (\sigma \nabla V) = 0, \quad (3.1)$$

where V [V] is the electrical potential and σ [S/m] is the electrical conductivity of the windings. Boundary conditions are set at their terminals by specifying the null potential condition. The outer surfaces of the coils are electrically insulated ($\mathbf{n} \cdot \mathbf{J} = 0$).

For the device with MNF, the expression describing M-H dependency can be linearized:

$$M = \alpha \arctan(\beta H) \approx \alpha \beta H = \chi H, \quad (3.2)$$

here, $\alpha = 7.668 \cdot 10^{-8}$ [A/m] și $\beta = 6,78 \cdot 10^{-4}$ [m/A] are empirical constants [37-42], and χ represents the magnetic susceptibility. Solving equation (3.1) will determine the distribution of current density and will result in the magnetic field source given by the mathematical model:

$$\nabla \times (\mu_0^{-1} \mu_r^{-1} \nabla \times \mathbf{A}) = \mathbf{J}, \quad (3.3)$$

where μ_0 [H/m] is the magnetic permeability of free space, μ_r is the relative magnetic permeability and \mathbf{A} [T·m] is the magnetic vector potential.

3.3.2 Determination of steady state circuit parameters

The calculation of the circuit parameters is performed energetically, in steady state, using the mathematical model from (3.1). The data are included in Table 3.1. The magnetic energy stored in the air gap is calculated as follows [30]:

$$W_{m,i} = \frac{1}{2} \mu_0 \left(\frac{N_i I_i}{b_w} \right)^2, \quad (3.4)$$

where N represents the number of turns of the winding considered, and b_w represents the distance, measured in meters, from the column to the ferrite housing. The wiring diagram describing the inductor is included in Figs. 3.3.

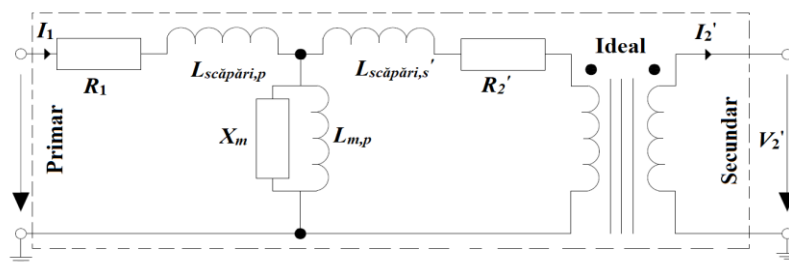


Fig. 3.3. Electrical equivalent circuit which models magnetic fluxes [42].

The mathematical model for the electromagnetic state in harmonic regime is:

$$(j\omega\sigma - \omega^2 \varepsilon_0 \varepsilon_r) \tilde{\mathbf{A}} + \nabla \times \left(\mu_0^{-1} \mu_r^{-1} \nabla \times \tilde{\mathbf{A}} \right) = 0, \quad (3.5)$$

where $\tilde{\mathbf{A}} = \mathbf{A} - j\omega^{-1} \nabla V$ represents the calibration condition. The mathematical model that characterizes the magnetic and electric field problem in *PWM* voltage supply is:

$$\Delta \mathbf{H} = \sigma \mu \frac{\partial \mathbf{H}}{\partial t}, \quad (3.6,a)$$

$$\Delta \mathbf{E} = \sigma \mu \frac{\partial \mathbf{E}}{\partial t}, \quad (3.6,b)$$

3.3.3 Numerical results of the simplified stationary transformer

The mathematical model used to solve the problem is (3.1) and (3.3).

Tabel 3.1 Transformer circuit parameters.

Parametrii de circuit	Valoare
$L_{11} = L_{22}$ [mH]	17.98
L_{12} [mH]	6.36
$L_{sc\acute{a}p\acute{a}ri, C.C.}$ [mH]	12.98
$L_{mag, C.C.}$ [mH]	0.76
$L_{sc\acute{a}p\acute{a}ri, PWM}$ [mH]	0.24
$L_{mag, PWM}$ [mH]	0.68

3.3.4 Numerical results of the transformer, powered by a PWM voltage source at 1 kHz

Three cases in the quasi-stationary regime are considered: close to the short-circuit mode, $R_s = 1 \mu\Omega$, an intermediate value R_s , close to the open-circuit mode, with $R_s = 1 M\Omega$. Figure 3.4 shows the induction of the magnetic field for the two values R_s .

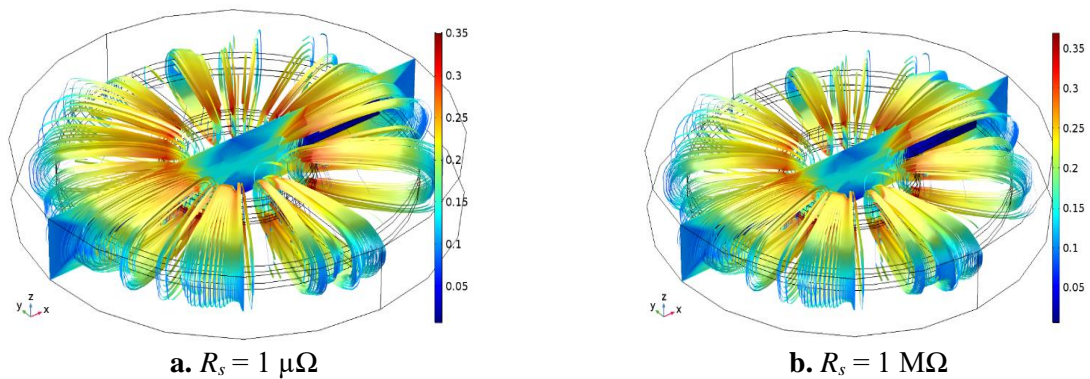


Fig. 3.4 Magnetic induction spectrum in quasi-stationary regime at $t = 0.284$ ms (end of *on* period).

Figure 3.5 shows the distribution of the magnetic field and the density of the Hertzian electric current density for different time moments, corresponding to the *on-off* interval.

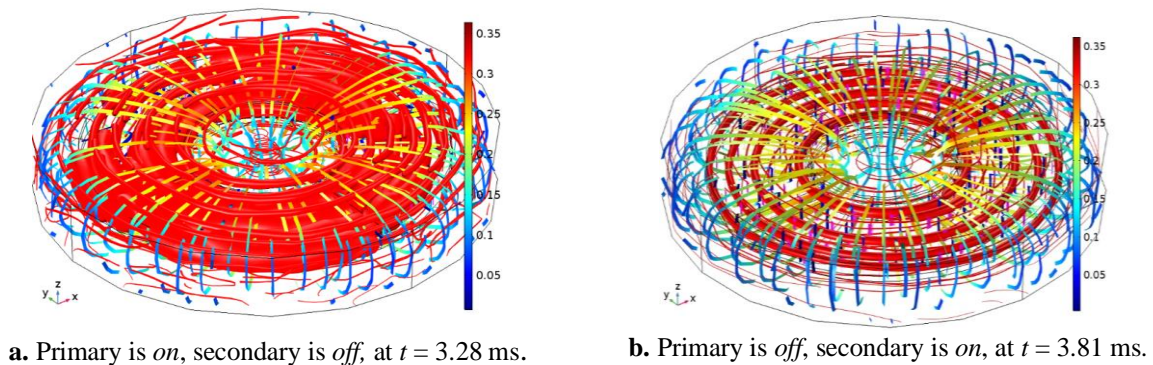


Fig. 3.5. Current density distribution (red tubes) and magnetic flux density. Values are in Tesla.

Planar transformers have magnetic cores, which allow fewer turns, so low values of resistances in alternating current, as well as low leakage inductances. The coil structure allows minimizing losses at high frequencies due to the current distribution on the conductor surface.

3.4 THE MODEL OF A FB MINIATURE, PLANAR, SIMPLIFIED INDUCTOR WITH MNF– CONCEPTUAL SIMPLIFIED MODEL

Two prototypes are considered: (A) – non-magnetic media, and (B) – MNF media.

3.4.1 Computational domain

In Figs. 3.6 shows the simplified geometry of the TFB, 1: 1. The windings are simplified, represented by cylindrical discs, made of circular, concentric turns.

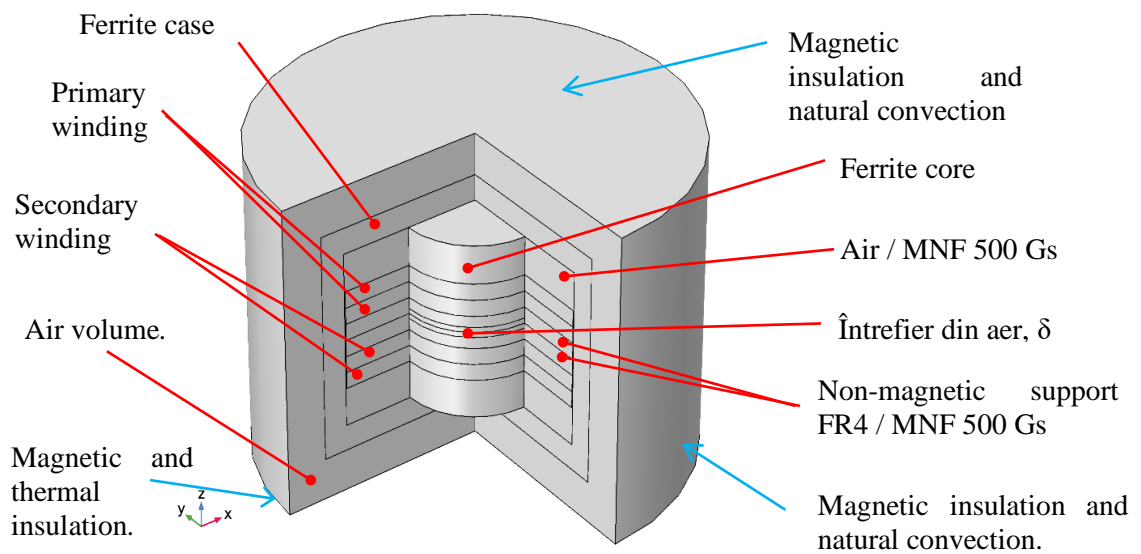


Fig. 3.6. Simplified computational domain of the FBT with different magnetic media and an air gap in the central column of the ferrite case. The windings are cylindrical discs. (1:1).

Figure 3.7 shows the equivalent electrical circuit for the *PWM* voltage supplied FBT at $f = 1$ kHz. The receiver is marked with a red dotted line.

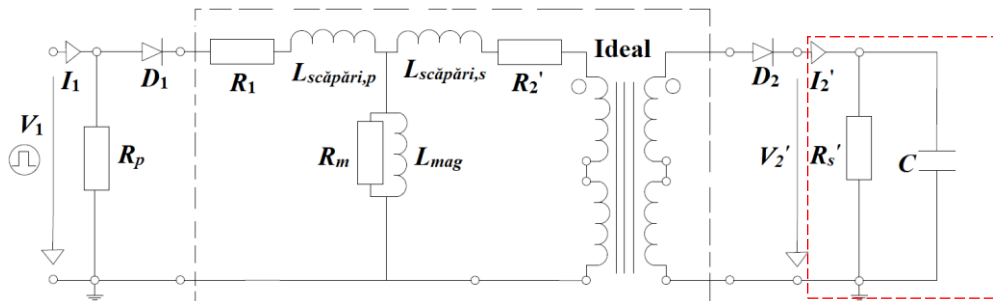


Fig. 3.7. Equivalent circuit at *PWM* supply voltage, V_1 , at frequency of 1 kHz, resistive-capacitive load, RC ($C = 0.03$ mF and $R = 1$ Ω).

3.4.2 Load circuit design for different constructive alternatives

The consumer, which connects to the terminals of the secondary, is represented by a light emitting diode, LED (light emitting diode), red in this case.

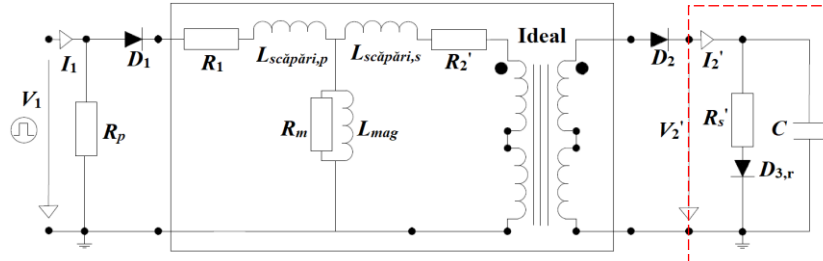


Fig. 3.8. Equivalent electrical circuit for PWM voltage supply, at 10 kHz, with load consisting of RC, and led, respectively ($C = 0.03$ mF, $R_s = 1$ Ω).

Figure 3.9 shows the electrical powers of the capacitor for different values of the load circuit elements determined in the *off* interval.

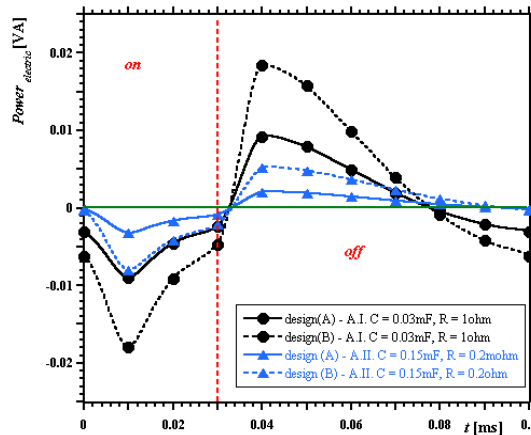


Fig. 3.9. Electrical power for (A) and (B) for I: $RC = 0.03$ ms, $R = 1$ Ω , $C = 0.03$ mF, respectively II: $R = 0.2$ m Ω and $C = 0.15$ mF.

Fig. 3.10 shows the dynamics of the stored magnetic energy in the air gap for model (A) - without MNF and different values of R and C , computed during the *on* sequence.

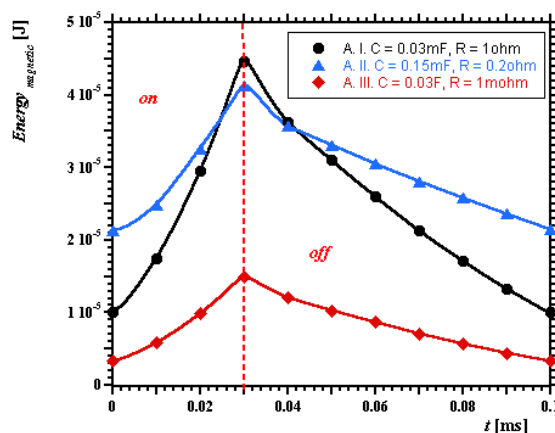


Fig. 3.10. Magnetic energy for (A) and (B) at (I) $R = 1$ Ω and $C = 0.03$ mF, (II) $R = 0.2$ m Ω and $C = 0.15$ mF, (III) $R = 1$ m Ω and $C = 0.03$ F.

By decreasing the load capacity value, C , the power increases, but the device does not discharge completely when the *off* interval begins, resulting in a secondary circuit out of sync with the *PWM* voltage.

3.4.3 Numerical simulation results for a miniature, simplified FBT in quasi-stationary mode, powered by a *PWM* voltage source at 10 kHz

Figure 3.11 shows the distribution of the magnetic field when the primary is *on* and the secondary is *off*, $\delta = 1$ mm, for both prototypes, (A) and (B).

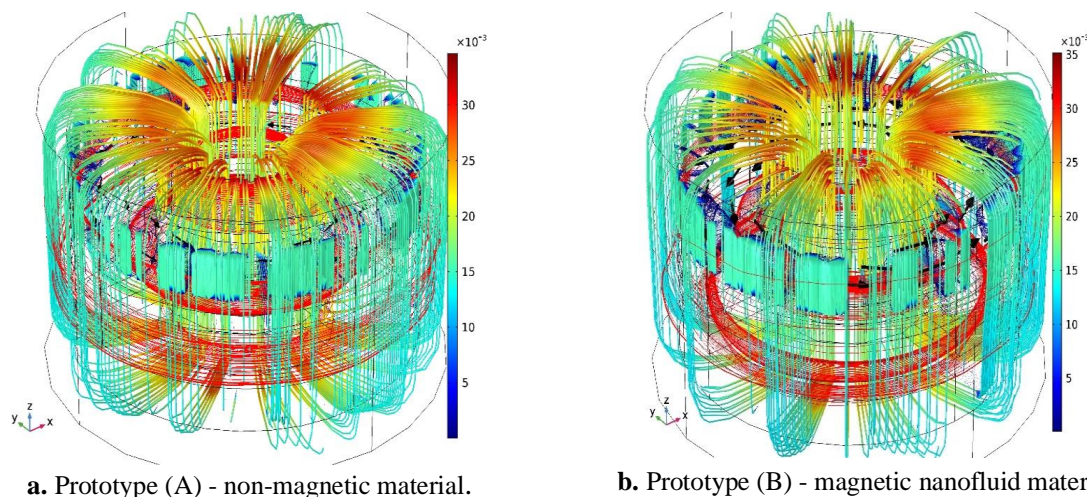


Fig. 3.11. Magnetic flux density, and Hertzian current density lines, $\delta = 1$ mm, different magnetic media, $C = 0.03$ mF and $R = 1 \Omega$, at $t = 0.13$ ms. Values are in Tesla.

The thermal field is described by the general law, in stationary form:

$$\nabla \cdot (k \nabla T) + \dot{Q} = 0, \quad (3.7)$$

where k [$\text{W} \cdot \text{m}^{-1} \cdot \text{K}^{-1}$] is the thermal conductivity, T [K] is the temperature and \dot{Q} [W/m^3] is the heat source (winding Joule losses). Current mean values are included in Tabel 3.2.

Tabel 3.2. Primary and secondary current mean values

δ [mm]	Prototipul (A)		Prototipul (B)	
	I_{primary} [A]	$I_{\text{secondary}}$ [A]	I_{primary} [A]	$I_{\text{secondary}}$ [A]
1	0.171	0.302	0.199	0.387
0.5	0.148	0.304	0.172	0.383
0.25	0.145	0.294	0.169	0.377
0.1	0.54	0.351	0.187	0.419

The heat source can be considered stationary. The MNF movement is neglected. An isothermal behavior with differences of up to one degree between model (A) and (B) is observed.

Distribuția puterii electrice de-a lungul circuitului de sarcină pentru $\delta = 0,25$ mm se prezintă în Fig. 3.34.

3.4.4 Numerical simulation results for the simplified TFB in quasi-stationary mode, at 100 kHz frequency

The results are presented for $f = 100$ kHz, $RC = 0.03$ ms and two cases: for case (I) with $C = 0.03$ mF and $R = 1 \Omega$, and (III) $C = 0.03$ F and $R = 1$ m Ω , respectively. For model (A), case (I) $C = 0.03$ mF and $R = 1 \Omega$, the magnetic energies have slightly higher values than (III), $C = 0.03$ F and $R = 1$ m Ω , where, regardless of size δ , the same peak value is kept. For model (B) - MNF, case (III), the values are higher than (I).

3.5 MINIATURAL FBT, WITH SPIRAL WINDINGS AT A FREQUENCY OF 10 KHZ, WITH DIFFERENT MAGNETIC MEDIA

3.5.1 Computational domain

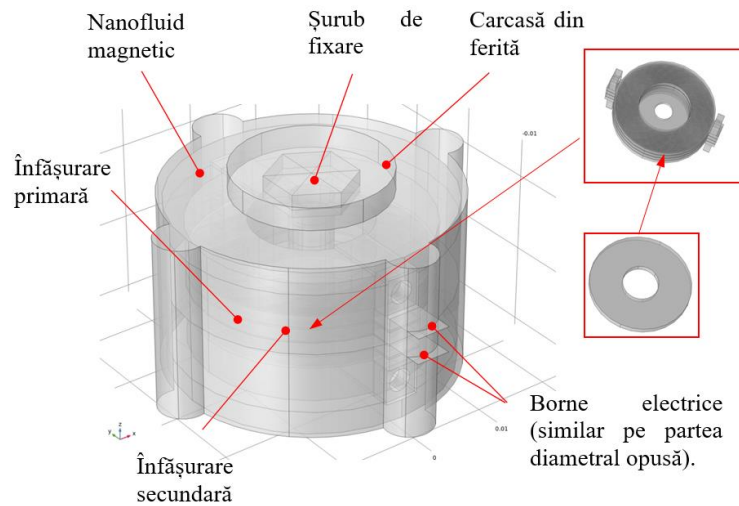
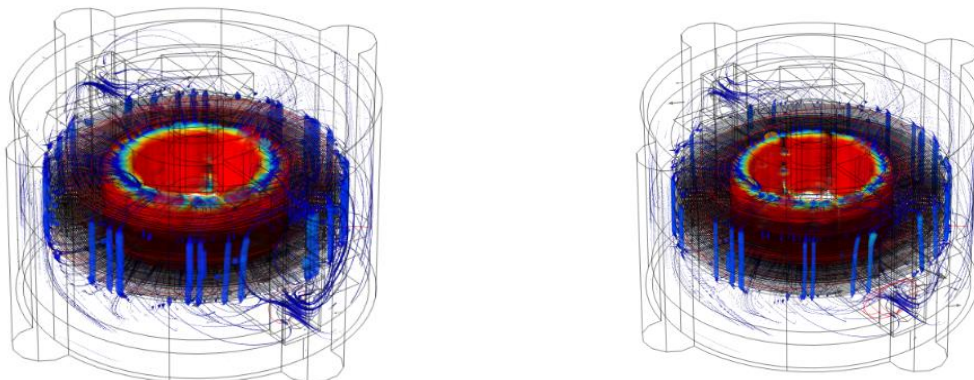


Fig. 3.12. Computational domain of the simplified FB inductor.

3.5.2 Numerical simulation results

Figure 3.13 shows the magnetic flux density for both models, with and without MNF.



a. Prototype (A) - non-magnetic material, $B_{max} = 1.2$ T. b. Prototype (B) – MNF material, $B_{max} = 1.8$ T.

Fig. 3.13. Magnetic flux density distribution and electric current density lines, for $\delta = 0.22$ mm, different magnetic media, $C = 0.03$ mF and $R = 1 \Omega$, at $t = 0.353$ ms.

Figure 3.14 shows the energy stored in the whole device for the model, (A) - without MNF, respectively (B) - with MNF, for different values δ .

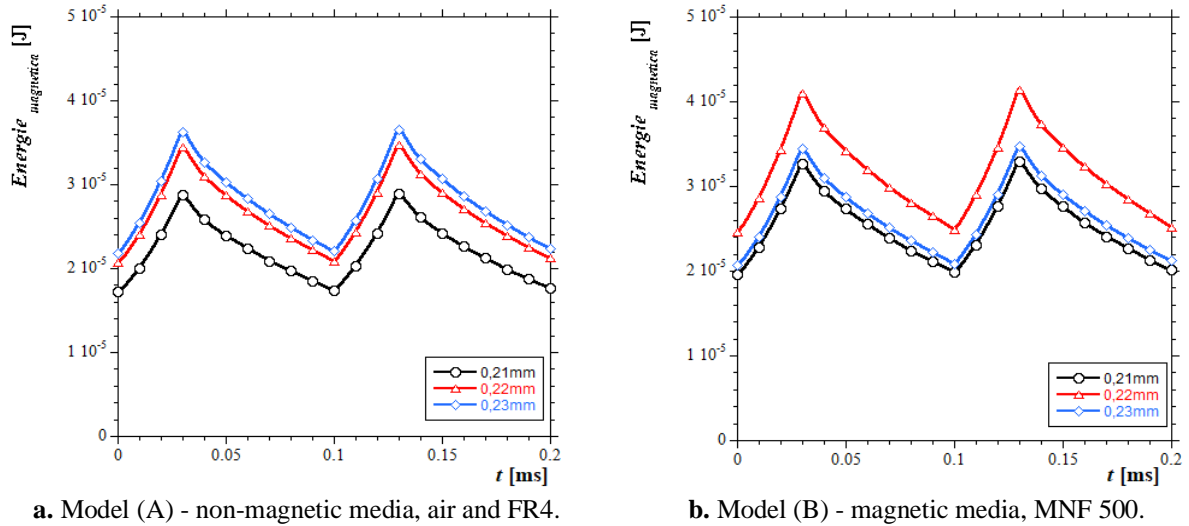


Fig. 3.14. Magnetic energy variations for both models and for different values of δ .

3.5 GALVANIC SEPARATION TRANSFORMER

The insulation between the primary and secondary winding minimizes the conduction phenomenon.

3.5.1 Galvanically isolated transformer in energy harvesting systems

The transformer is provided with a shielding film for limiting leakage flows, located between the windings and the base support, made of a soft magnetic material

3.5.2 Computational domain

A single-phase, simplified, low power, 1:1 transformer, at sine voltage $V_1 = 20$ V, at frequency $f = 50$ Hz, in transient mode, with $R_s = 100 \Omega$ is analyzed. The equivalent electrical circuit is shown in Fig. 3.15 together with the computational domain.

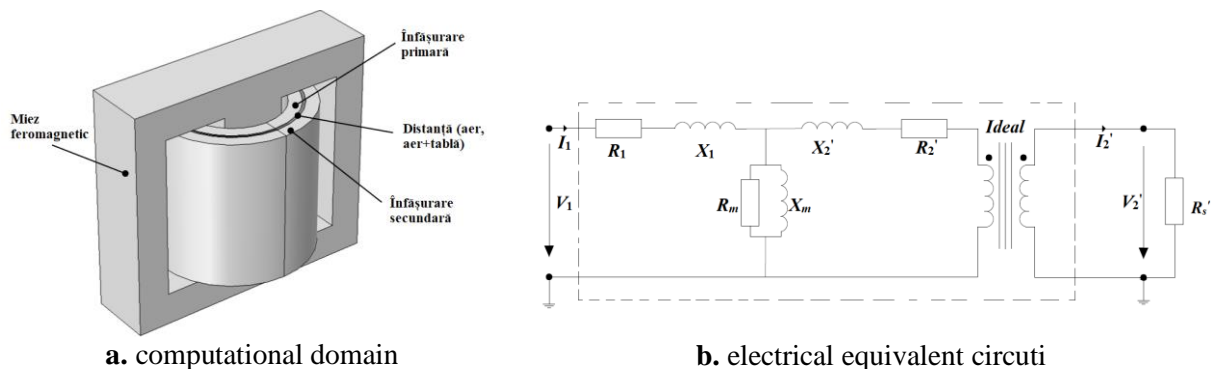


Fig. 3.15. Computational domain and electrical equivalent circuit that models the magnetic fluxes for the low power transformer studied [43].

Consider different distances between the windings, d. Consider a second model that has a magnetic screen at half distance. The last case considers $d_6 = 6$ mm and varies the

position of the screen in relation to the windings. For the transformer core a nonlinear dependence relation is used between the magnetic induction, \mathbf{B} and the magnetic field strength, \mathbf{H} , given by the relation:

$$\mathbf{H} = f(|\mathbf{B}|) \frac{\mathbf{B}}{|\mathbf{B}|}, \quad (3.8)$$

For the calculation of the magnetization reactance, X_m , the magnetic energy stored in the volume of the core is used for the calculation of the magnetization inductance.

$L_m = \frac{2}{I^2} \int_V \frac{\mathbf{H} \cdot \mathbf{B}}{2} dV$ [44] and subsequently it is used in the reactance calculation formula, $X = \omega L$.

3.5.4 Numerical simulation results

The resistance and reactance values are calculated and included in Table 3.3 These are calculated based on a transient regime, at frequency $f = 50$ Hz, and voltage $V_1 = 20$ V.

Tabelul 3.3 The values of resistances and reactances for different dimensions of the distance between the windings, with and without magnetic screen.

d [mm]	with air					with air and magnetic shield				
	$R_1[\Omega]$	$R_2[\Omega]$	$X_1[\Omega]$	$X_2[\Omega]$	$X_m[\Omega]$	$R_1[\Omega]$	$R_2[\Omega]$	$X_1[\Omega]$	$X_2[\Omega]$	$X_m[\Omega]$
1	0.812	1.057	53.92	79.772	282.84	0.781	1.042	53.26	78.61	280.45
2	0.812	1.061	53.76	78.841	282.051	0.781	1.066	52.79	77.97	279.82
3	0.812	1.079	53.45	78.542	281.91	0.781	1.085	52.45	77.49	279.58
4	0.812	1.098	53.03	78.356	281.73	0.781	1.112	52.52	77.63	279.71
5	0.812	1.108	52.88	78.014	281.46	0.781	1.133	52.57	77.72	279.84
6	0.812	1.112	52.64	77.896	281.18	0.781	1.168	52.69	77.84	279.98

Table 3.4 shows the parameter values for the third case and for two dimensions of the magnetic screen (0.4 mm and 0.05 mm, respectively).

Tabel 3.4 The resistance and reactance values for different dimensions of the distance of the screen from the primary winding and its two thicknesses.

d [mm]	0.4 mm					0.05 mm				
	$R_1[\Omega]$	$R_2[\Omega]$	$X_1[\Omega]$	$X_2[\Omega]$	$X_m[\Omega]$	$R_1[\Omega]$	$R_2[\Omega]$	$X_1[\Omega]$	$X_2[\Omega]$	$X_m[\Omega]$
0	0.773	1.1915	54.47	80.66	284.36	0.781	1.1618	53.29	79.04	283.85
1	0.773	1.1915	54.11	80.48	284.01	0.781	1.1641	53.46	79.70	283.62
2	0.773	1.1921	54.02	80.60	283.82	0.781	1.1624	52.67	78.75	283.37
3	0.773	1.1952	54.56	81.61	283.57	0.781	1.1639	52.83	79.17	283.54
4	0.773	1.1957	54.39	81.64	283.22	0.781	1.1641	52.63	79.09	283.68
5	0.773	1.195	53.99	81.36	283.04	0.781	1.1641	52.46	79.08	283.47
6	0.773	1.1944	53.64	81.17	282.87	0.781	1.640	52.21	79.05	283.53

The simulated model is working in load conditions, at $R_s = 100 \Omega$, the excitation of the coils is in voltage, and the value of the supply voltage, sinusoidal at $V_1 = 25$ V, and $f = 50$ Hz, as long as the waveforms do not deform, keeping their appearance sinusoidal, the ferromagnetic core does not saturate.

3.6 CONCLUSIONS

The use of strong magnetic media causes high values of magnetic energy and functions as an additional coupling factor between the windings. When dimensioning the load circuit, the RC time constant must be taken into account, as well as the duty factor.

CHAPTER 4 STORAGE OF HARVESTED ENERGY

4.1 INTRODUCTION

The total energy must be greater than the energy consumed. In designing EH systems, the storage capacity and the total consumption must be known beforehand.

4.2 ENERGY STORING DEVICES

The energy supply device choice is made taking into account the need and energy constraints imposed at the level of the application or assembly to be supplied.

4.2.1 Batteries

The most used batteries are zinc, lithium and alkaline. Zinc ones have the highest energy density, 3780 J / cm^3 , but the lowest lifetime compared to lithium, with 2880 J / cm^3 , and alkaline ones, with 1200 J / cm^3 and an intermediate life [45].

4.2.2 Supercapacitors

SC have low internal impedance values, long lifetimes, but have a low energy density and a fast self-discharge speed of up to 5.9% per day.

4.2.3 Other energy storage devices

The development of microbatteries is due to the smaller size of the nodes that require proper integration, the main obstacle is the reduced output power.

The inversely proportional dependence of the voltage-current makes it quite difficult to integrate combustion micropiles in the supply stage without additional electronic circuits. The integration of small-scale thermal micromotors was difficult to achieve. Due to the use of silicon in the microfabrication stage, obstacles were removed and values of approx. 10-20 W were reached for efficiencies of 5-20% [29,45].

4.3 COMPACT, INTERDIGITATED SUPERCAPACITOR SYSTEMS

4.3.1 Supercapacitors with carbon nanotubes

CL is applied to improve the performance of planar SCs with interdigitated electrode configuration [46]

4.3.2 Computational domain

Figure 4.1 shows the initial shape of the elemental cell.

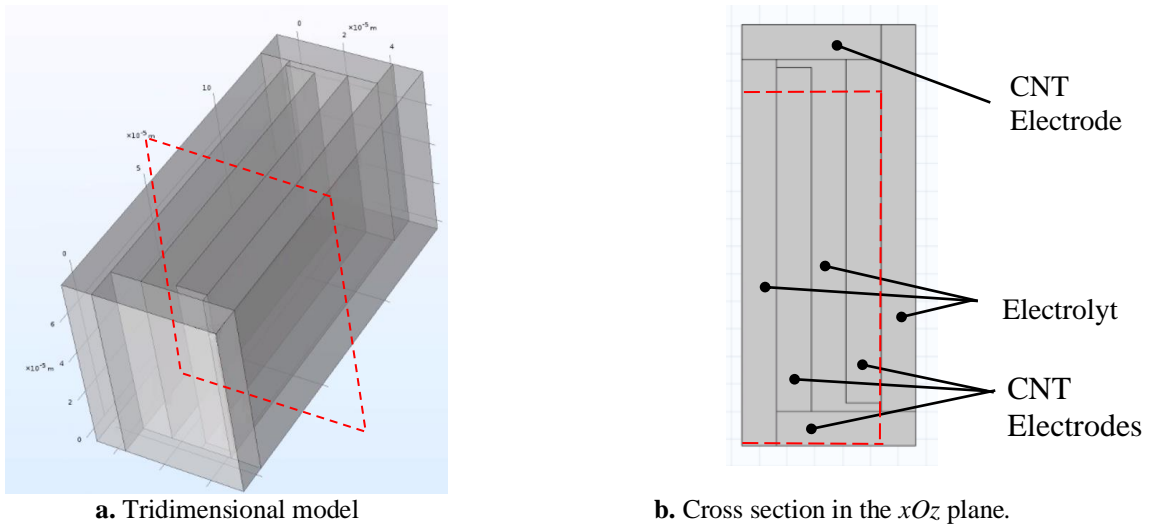


Fig. 4.1. The elemental cell, after [46]. The dimensions are in meters.

Its capacity can be calculated using stationary operating conditions, while the electrical resistance can be characterized by electrokinetic operating conditions.

4.3.3 Numerical simulation results

Shape factor (FF) H/L (height / length) is used. CNT is divided into pairs. Figure 4.2 shows the electrical capacity, respectively the maximum capacities obtained depending on the FF and the number of pairs [46].

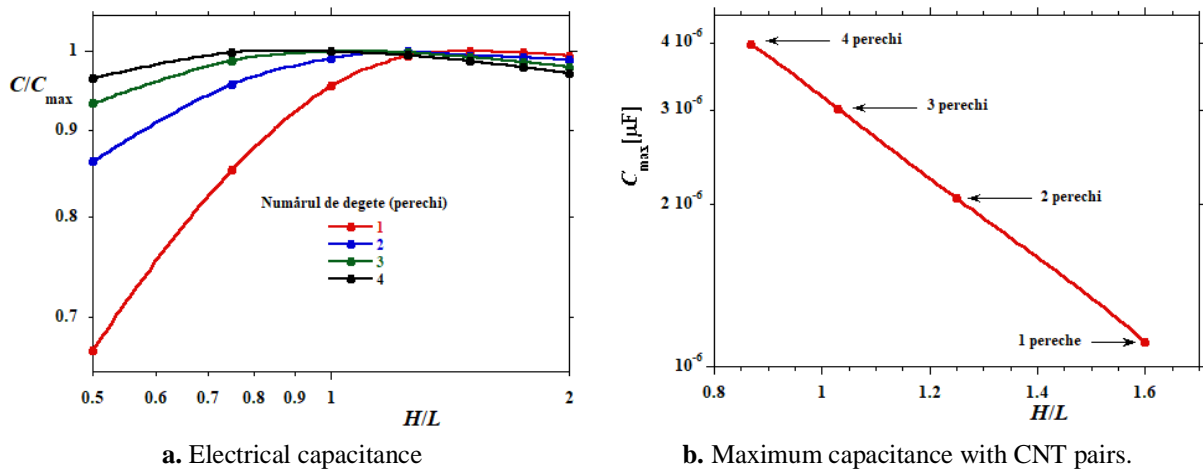


Fig. 4.2 The first optimization sequence [146].

Similar, Fig. 4.3,a shows the electrical resistance of the elemental cell as a function of FF, and for Fig. 4.3, b the variation of the time constant in relation to the shape factor.

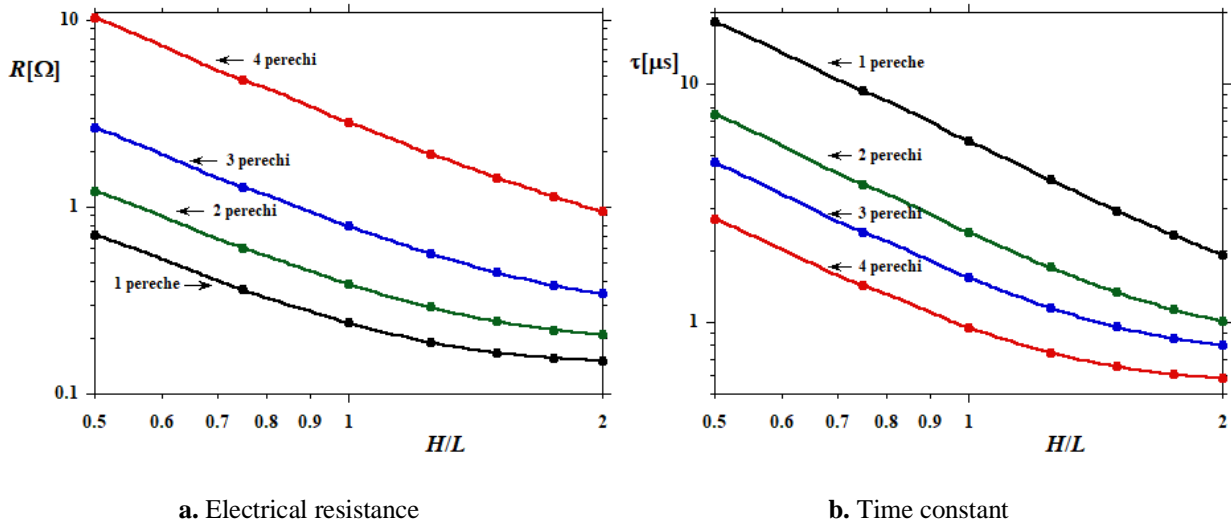


Fig. 4.3. The electrical resistance, and the time constant, respectively, of the optimal elemental cell depending on the number of NTC blocks. The second optimization sequence.

The optimal cell structure also takes into account the time constant, $t = RC$.

4.3.4 Higher order ensembles

The first four higher order assemblies obtained by successive mirrors of the elementary cell are presented. The assembly strategy is based on parallel, successive connections of lower-order assemblies to higher-order ones.

4.3.5 Conclusions

CL is applied to improve the performance of planar supercapacitor with CNT electrodes and interdigitated electrode configurations. The CNT and the electrolyte between them are represented by homogeneous blocks with relative anisotropic permittivities. The only variable in the optimization sequence is FF. The maximum capacity is proportional to the number of NTCs. Resistance decreases monotonously with FF

4.4 CONCLUSIONS

For the particular case, wireless sensor nodes, the storage stage cannot miss. The use of SC optimization sequences aims to achieve higher values of energy density for the same operating advantages.

CHAPTER 5 WIRELESS SENSOR NETWORKS

5.1 INTRODUCTION

EH advantages involve the reduction or elimination of battery costs and their maintenance, the automatic warning of the nodes regarding the available energy (energy aware), respectively the management of the available energy resources.

5.2 WIRELESS SENSOR NODES

5.2.1 Main components of wireless sensor nodes

The basic components [47] of a wireless sensor node are shown in Figure 5.2. The simplest structure of a node can be reduced to the following components:

- Transmitter – receiver (Radio – Frequency);
- microcontroller (MCU) 8 bit;
- supply source and sensor;
- other passive additional circuits.

RF transmitters must have an adjustable output power (allowing the optimization of the transmission power) accessed through the memory registers.

Node tasks are coordinated by the MCU. MCU used in WSN will have standby currents of approx. 1 μ A, short wake-up time and the ability to interface with a wide range of peripherals.

. Emițătoarele RF trebuie să aibă o putere de ieșire reglabilă (care să permită optimizarea puterii de transmisie) accesată prin intermediul registrelor de memorie. Au fost dezvoltate o serie de soluții pe un singur cip, care încorporează un MCU și un emițător-receptor radio [136].

5.2.2 Wireless sensor nodes characteristics

- Lifetime
- Energy consumption
- Idle time
- Precision
- Error tolerance
- Scalability
- Network capacitance
- Success rate

WSNs are complex systems, consisting of a number of nodes that incorporate MCUs and peripherals that usually communicate via RF, the consumption is 100 μ W-10 mW. Communication in WSN is usually done in a short range, from 10 m ... 100 m.

5.2.3 Network topologies

The routing scheme (transmission) can be classified into: directly, in several jumps or in several jumps, in groups [48]. Figure 5.1 illustrates different network topologies, where S represents the wireless sensors, C is the coordinating node, central, and R are routers.

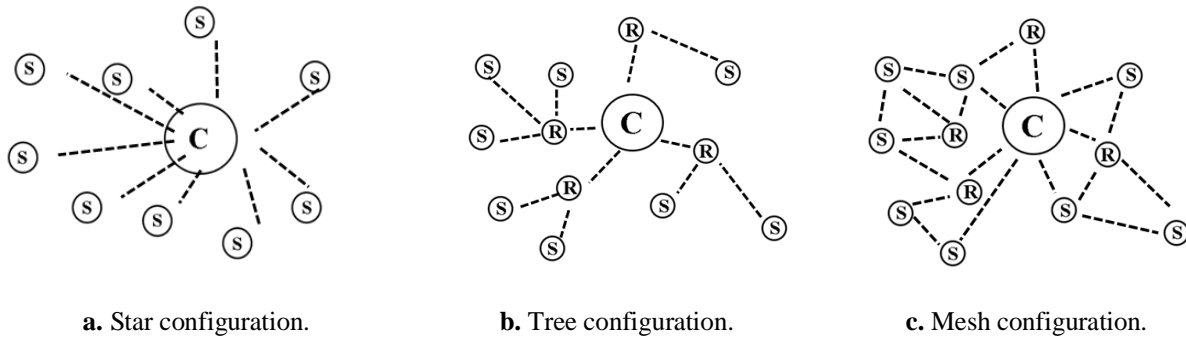


Fig. 5.1 Network topologies for wireless sensor nodes.

It is important to note that the star configuration network can only have one central node which makes it vulnerable in case of failure.

5.3 WIRELESS SENSOR NETWORK SIMULATION

5.3.1 Network configuration

The configuration of the network consisting of 50 nodes and an RF transmission-reception antenna arranged randomly on an area of $400 \times 400 \text{ m}^2$ is shown in Fig. 5.2.

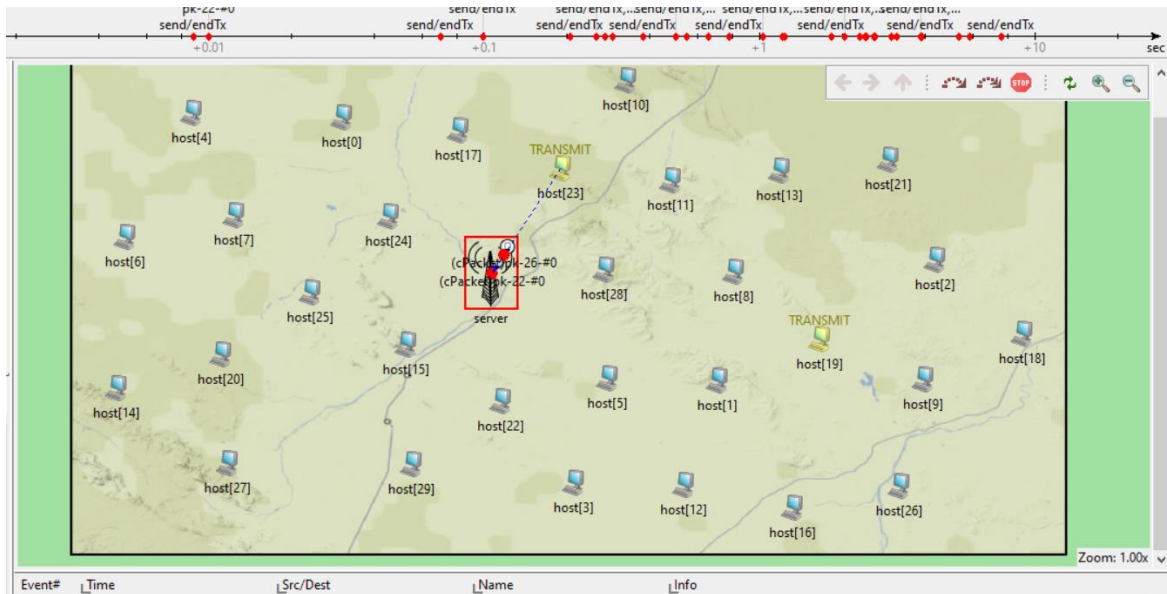


Fig. 5.2. Configuration of a WSN with 50 nodes and a transmitting-receiving station. After communicating the measured data, the transmitting nodes become inactive.

5.3.2 Simulation results

Figure 5.3 shows the number of active nodes in the interval of 50 cycles for the network with 30 nodes, and with 50 nodes, respectively. A cycle consists of 1000 ms.

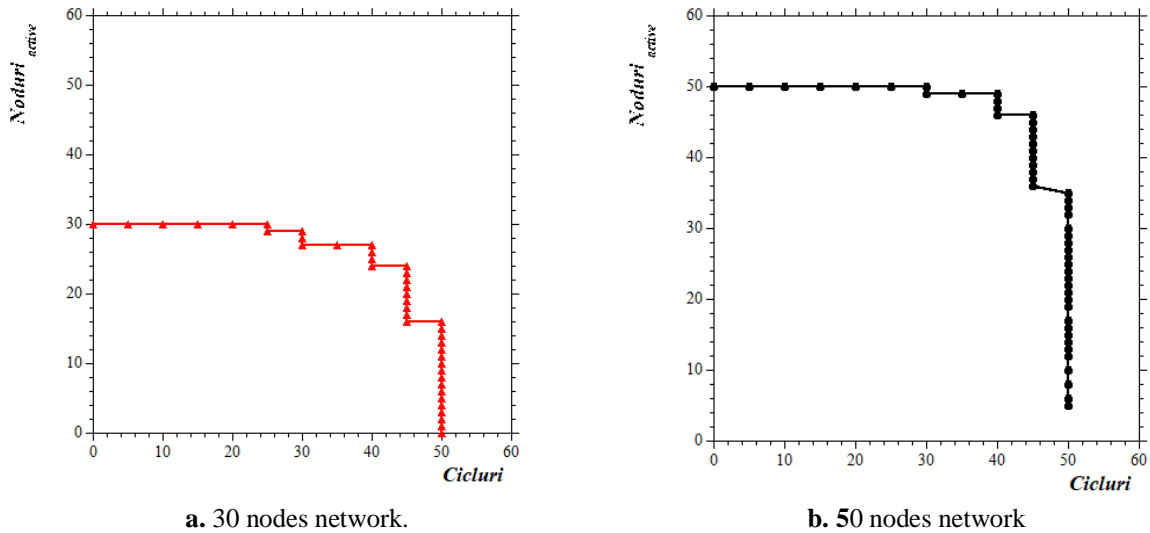


Fig. 5.3. Number of active nodes in the range of 50 cycles, corresponding to 50 s, located on an area of $400 \times 400 \text{ m}^2$, for both WSN networks.

The data packets have the size of 1500 bits, and the transmitted messages have a size of 500 bits. Fig. 5.4 shows the variation of the average consumed energy for both considered cases, over an interval of 50 cycles, corresponding to 50 s.

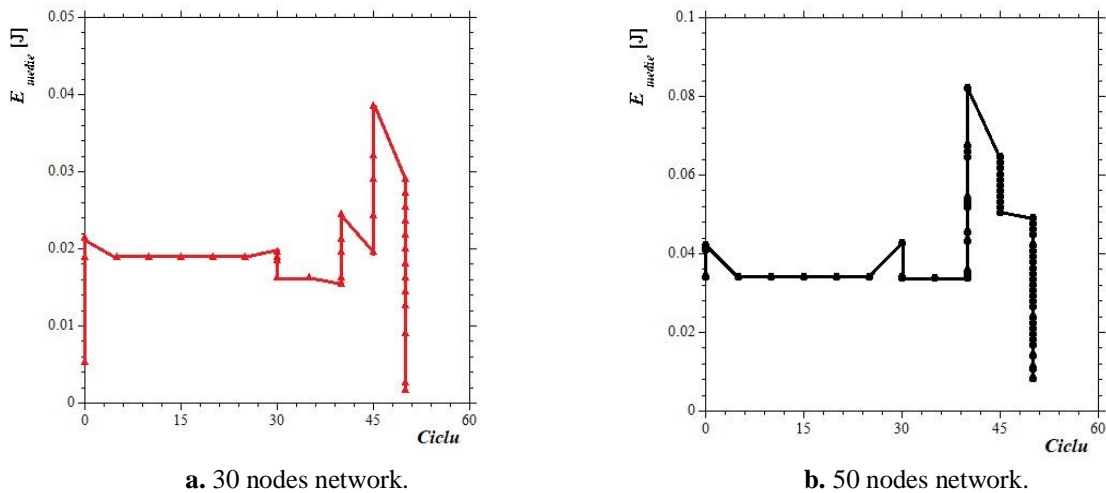


Fig. 5.4. Average energy consumption over 50 cycles, corresponding to 50 s, of WSN nodes located on an area of $400 \times 400 \text{ m}^2$, for both case considered.

The network scalability characteristic is observed.

5.3.3 Conclusions

It is preferable that the WSN to be designed in such a way that the packet transmission is done at minimum consumption. Single-hop direct protocols have the disadvantage of transmitting data one at a time, regardless of distance and without involving other nodes. The distance between the sensors and the central node dictates the energy consumption, which for

the data transmission the nodes in the immediate vicinity is minimal. Consumption increases when more data is transmitted.

GENERAL CONCLUSIONS, CONTRIBUTIONS AND FUTURE PERSPECTIVES

C1. GENERAL CONCLUSIONS

The thesis presents, in the form of a general energy harvesting system, a series of methods and models of energy conversion for low power applications, the final consumer being represented by the nodes of a wireless sensor network.

Various energy sources, harvesting methods and materials used in energy conversion were presented. There are three devices in the block of the primary mechanical-electrical converters that can be used in EH systems. The first device is a piezoelectric converter, scalable, used in various joints. Two constructive models are presented.

The second device is a MSA that has the property of reversibility. The results obtained for MSA, in voltage and in *PWM* current supply at $f_{PWM} = 100$ Hz are compared. The effect of friction between the moving parts is also evaluated, and, for *PWM* voltage excitation, when friction is neglected, the mechanical spring is introduced, by F_{PS} , which determines the return to the initial position of the drive rod. A spectral analysis is performed by calculating the electrical frequencies, f_e , specific to the *PWM* supply frequency, f_{PWM} , and the eigenfrequencies, f_m , respectively and also the rod displacement frequencies, f_d , analysis necessary for the stable operation of MSA. The secondary harmonics, that appear in the displacement of the rod, which destabilize the MSA functioning, are eliminated by increasing the pre-stress level, by considering f_e and f_m . Adjustment to f_{PWM} is a compromise that results in reduced displacement amplitudes.

The last mechanical-electrical converter is a device that uses the deformation of the walls of an arterial vessel to move a fluid with high electrical conductivity in a stationary magnetic field. A load resistor is connected to the electrode terminals.

A transformer with an air gap in the central column of the ferromagnetic core is modeled. The operation in stationary regime, and in *PWM* voltage, at the frequency $f = 1$ kHz, respectively is analyzed, with the filling factor $D = 0.3$ for which the open-circuit, short circuit and load operation is modeled. The circuit parameters are calculated.

A *PWM* voltage supplied FB inductor, at $f = 10$ kHz, with cylindrical windings is modeled, model (A) with non-magnetic media and (B) with MNF. The stored magnetic energy for different values of the air gap is analyzed. The optimal value for δ is determined. A thermal study is performed in stationary conditions. The secondary circuit is designed.

Numerical simulation is also performed for the unsimplified model with spiral windings at $f = 10$ kHz. It is found that the size of the air gap for which we have the maximum energy value is around $\delta = 0.22$ mm for the model (B) - with MNF.

A 1:1 galvanic isolation transformer at $f = 50$ Hz and at 20 V, alternating voltage, is analyzed. The results are presented for the case when we only have air between the windings

and when, at half the distance, d , a magnetic screen is inserted. The winding distances are varied from 1 mm ... 6 mm, when the secondary reaches the core, for both versions (without and with screen). For the case when both air and magnetic screen is considered, an harmonic regime is also analyzed. The resistances and reactances of the primary and secondary winding, respectively are calculated using energy methods. The circuit parameters are also computed when the screen is considered attached to the primary winding, and, from mm to mm, when moving to the secondary one. Here, the maximum distance between the windings, 6 mm and two screen sizes is considered.

Different configurations for the WSN nodes are presented, and for the mesh configuration a network with 50 and 30 nodes, respectively, placed randomly on an area of $400 \times 400 \text{ m}^2$ is analyzed. The transmission protocol is multi-hop.

C2. ORIGINAL CONTRIBUTIONS

The study of the mechanical-electrical converter for harvesting biomechanical energy by using piezoelectric materials and the rotational movement of the elbow joint.

The electromagnetic and spectral analysis, by calculating the eigenfrequencies, the electrical and displacement frequencies, of a MSA powered from a PWM voltage source at $f_{PWM} = 100 \text{ Hz}$, with a duty cycle of $k = 30\%$ for which the optimal level of prestress is established by introducing the mechanical spring for a stable operation. The results obtained at current excitation are compared with those obtained at voltage excitation. Subsequently, the friction effect at the upper coupling level (drive rod, steel intermediate piece and upper plate of the Fe housing) is also considered. Spectral analysis neglects friction.

The study of an implantable mechanical-electrical converter that uses the deformation field of the arterial walls to set in motion, in a stationary magnetic field, a fluid with a strong electrical conductivity in compartments located outside the blood vessel. The physical field of calculation is taken from the specialized literature. The open circuit and short-circuit modes for a resistance load connected to the electrical terminals are analyzed.

Development of numerical models, with gradual complexity, of flyback electrical inductors. A study to optimize the dimensions of the air gap is performed. The influence of using strong magnetic media in FBT construction is analyzed.

Designing a wireless sensor network and a multi-hop data transmission protocol in OMNET ++ for which the available energy of nodes is calculated after data packet transmission

C3. FUTURE PERSPECTIVES

Using the CAD construction model for the knee joint prosthesis and the converter, for which a numerical modeling has already been performed, in a unitary assembly. Numerical analysis of the transmission of the rotational movement from the prosthesis to the device.

Designing the MS generator by reversing the operation of the MSA and performing a thermal analysis.

Development and study of new circuits, of different complexities, of energy conversion for flyback inductors to maximize harvested energy and minimize losses.

Development and study of a new galvanic separation transformer for a screen composed of strong electrical conductive material (copper) and weak electrical conductive material (magnetic screen already used in simulation).

Extending numerical studies to other devices that use other energy sources.

Development of numerical models for energy storage devices and their structural and constructive optimization.

Development of new wireless sensor networks and improvement or implementation of new data transmission protocols to minimize energy consumption.

ANEXE

C++ code for sensor nodes and energy consumption calculus.

BIBLIOGRAFIE

- [1] A. Bejan, J. Peder Zane, "Design în natură, cum guvernează legea constructală evoluția în biologie, fizică, tehnologie și organizarea socială", Editura Agir, 2013, ISBN: 978-973-720-476-9.
- [2] A. Bejan, S. Lorente, "Teoria constructală", Editura Agir, 2011, ISBN: 978-973-720-293-2.
- [3] A.M. Morega, "Sisteme fotovoltaice. Monografie", notițe de curs, https://curs.upb.ro/pluginfile.php/303328/mod_resource/content/1/Monografie_SFV.pdf, accesat la data de 24.11.2020.
- [4] G. Balasubramanian, S. Singaravelu, "Fuzzy logic controller for the maximum power point tracking in photovoltaic system", *International Journal of Computer Applications (0975 – 8887)*, Vol. **41**, No.12, March 2012.
- [5] M. Banj-Hani, M.A. Karami, Energy harvesting from mastication forces via a smart tooth, DOI: 10.1117/12.2219390.
- [6] A. Nandaa, M.A. Karami, "Energy Harvesting from arterial blood pressure for powering embedded brain sensors", *Sensors and Smart Structures Technologies for Civil, Mechanical, and Aerospace Systems 2016*, doi: 10.1117/12.2219234.
- [7] A. Nandaa, M.A. Karami, "Energy harvesting from arterial blood pressure for powering embedded micro sensors in human brain", *Journal of Applied Physics 121*, 124506 (2017); <https://doi.org/10.1063/1.4977842>.
- [8] A. Nandaa, M. A. Karami, "Energy harvesting from arterial blood pressure for embedded brain sensing", *ASME 2016 International Design Engineering Technical Conferences and Computers and Information in Engineering Conference*, DOI: 10.1115/DETC2016-60573.
- [9] L.B. Kong, T. Li, H.H. Hng, F. Boey, T. Zhang, S. Li, "Waste energy harvesting, mechanical and thermal energies", DOI: 10.1007/978-3-642-54634-1, ISBN 978-3-642-54633-4, Springer Heidelberg New York Dordrecht London.
- [10] Y. Veli, A.M. Morega, „An energy harvesting device for portable applications”, *Scientific Bulletin, University Politehnica of Bucharest, Romania, în curs de publicare*.
- [11] Y. Veli, A.M. Morega, "Generator piezoelectric pentru aplicații de putere redusă", *Simpozionul de Mașini Electrice SME'16*, 11 Noiembrie 2016, București, România.
- [12] M. Popa, A.M. Morega, L. Pîslaru-Dănescu, M. Morega, Y. Veli, "The optimization of the active magnetic material in a magnetostrictive actuator provided with a supplementary electric bias, (in Romanian) *Electrical Machines, Materials, and Drives Present and Trends, SME'18*, Bucharest, 2018.
- [13] Y. Veli, A.M. Morega, L. Pîslaru-Dănescu, M. Morega, "Numerical simulation analysis of a linear magnetostrictive actuator", *Rev. Roum. Sci. Techn.– Électrotechn. et Énerg.* Vol. **65**, 3–4, pp. 157–164, Bucharest, 2020.
- [14] U. Ahmed, J. Harju, J. Poutala, P. Ruuskanen, P. Rasilo, R. Kouhia, "Finite element method incorporating coupled magneto-elastic model for magneto-mechanical energy harvester", *Conference: Compumag*, Daejeon, Korea, June 2017. - 80
- [15] Z. Deng, M.J. Dapino, "Multiphysics modeling and design of Galfenolbased unimorph harvesters", *Proc. of SPIE, The Int. Soc. For Optical Eng.*, 9433, April 2015.
- [16] B. Rezaealam, T. Ueno, S. Yamada, Quasi-static finite element analysis of magnetostrictive vibration energy harvester, *J. Magn. Soc. Japan*, 36, 3, 2012.

- [17] L. Pîslaru-Dănescu, A.M. Morega, M. Morega, "A novel magnetostrictive actuator based on new giant magnetostrictive materials", *IEEE Int. Symp. Adv. Topics El. Eng.*, Bucharest, 2011.
- [18] M. Popa, A.M. Morega, L. Pîslaru-Dănescu, M. Morega, "Magnetostrictive actuator – a bi-dimensional analysis", (in Romanian), Electrical Machines, Materials and Drives, Present and Trends, SME'16, Bucharest, 2016.
- [19] J.R. Downing, S.-M. Na, A.B. Flatau, Compressive prestress effects on magnetostrictive behaviors of highly textured Galfenol and Alfenol thin sheets, *AIP Advances*, 7, 056420, 7 pp., 2017.
- [20] D.C. Jiles, D. L. Atherton, Theory of ferromagnetic hysteresis, *J. of Magn. Magn. Mat.*, **61**, pp. 48–60, 1986.
- [21] D. C. Jiles, "Theory of magneto-mechanical effect", *J. Phys., D, Appl. Phys.*, **28**, pp. 1537–1546, 1995.
- [22] Y. Liu, X.I Gao, C. Chen, "Research of Jiles-Atherton dynamic model in a giant magnetostrictive actuator", *Math. Probl. in Eng.*, Hindawi Pub. Corp., Article ID 2609069, 2016.
- [23] F.T. Calkins, "Design, analysis, and modeling of giant magnetostrictive transducers", Iowa State Univ. Capstones, Theses, and Dissertations, 1997.
- [24] J.G. Benatar, A.B. Flatau, "FEM implementation of a magnetostrictive transducer", *Smart Struct. Mat. Smart Struct. Integrated Syst.*, Ed. A.B. Flatau, *Proc. of SPIE*, 5764, pp. 482–493, SPIE, Bellingham, WA, 2005.
- [25] T. Fukuda, H. Hosokai, H. Ohyama, "Giant magnetostrictive alloy (GMA) applications to micro mobile robot as a micro actuator without power supply cables", *Proc. IEEE Micro Electro Mech. Systems*, pp. 210–215, 1991.
- [26] A. Pfenniger, V.M. Koch, A. Stahel, R. Vogel, "Energy harvesting from variation in blood pressure through deformation of arterial wall using electro-magneto-hydrodynamics", *Excerpt from the Proceedings of the COMSOL Conference*, 2010, Paris.
- [27] A. Pfenniger, L.N. Wickramarathna, R. Vogel, V.M. Koch, "Design and realization of an energy harvester using pulsating arterial pressure", *Med Eng Phys* (2013), <http://dx.doi.org/10.1016/j.medengphy.2013.01.001>.
- [28] A. Pfenniger, D. Obrist, A. Stahel, V.M. Koch, R. Vogel, "Energy harvesting through arterial wall deformation: design considerations for a magneto-hydrodynamic generator", *Med Biol Eng Comput* (2013) 51:741–755, DOI 10.1007/s11517-012-0989-2.
- [29] S.Priya, D.J. Inman, "Energy harvesting technologies", Springer, DOI 10.1007/978-0-387-76464-1.
- [30] L. Dixon, "Designing Planar Magnetics", Texas Instruments, Topic 4, pp. 4-23.
- [31] L.H. Dixon, Jr., "Design of flyback transformers and filter inductors, filter inductor and flyback transformer design for switching power supplies", TI, 2001.
- [32] Texas Instruments, Section 5 Inductor and Flyback, Transformer Design.
- [33] L.H. Dixon, "Transformer and inductor design for optimum circuit performance", Topic Category: *Magnetic Component Design*, TI, 2011.
- [34] J. Picard, "Under the hood of flyback smps design", TI Literature Number: SLUP261, TI, 2010.
- [35] A. Fagnani, "Isolated continuous conduction mode flyback using the TPS55340", Texas Instruments.
- [36] **Y. Veli**, A.M. Morega, L. Pîslaru-Dănescu, M. Morega, Planar transformer for energy harvesting applications, *Scientific Bulletin, University Politehnica of Bucharest*, în curs de publicare.
- [37] **Y. Veli**, A.M. Morega, L. Pîslaru-Dănescu, M. Morega, 'Numerical modeling of a flyback converter with different magnetic media, for micro-power controllers', *ICATE 2018*, Craiova, România.

- [38] J.B. Dumitru, A.M. Morega, L. Pîslaru-Dănescu, M. Morega, "High frequency miniature planar transformer for energy harvesting applications", *EPE*, 2016, Iași, România.
- [39] L. Pîslaru-Dănescu, A.M. Morega, J.B. Dumitr, M. Morega, N.C. Popa, F.D. Stoian, D. Susan-Resiga, S. Holotescu, M. Popa, "Miniature planar spiral transformer with hybrid, ferrite and magnetic nanofluid core", *IEEE Transactions on Magnetics*, vol. **54**, 10, Article Number: 4600614, October 2018, DOI: 10.1109/TMAG.2018.2864162, WOS: 000445253900001.
- [40] R.N. Ramakoteswaa, L. Gahane, S.V. Ranganayakulu, "Synthesis, applications and challenges of nanofluids – review", *Journal of Applied Physics (IOSR-JAP)*, 21-28, 2014.
- [41] **Y. Veli**, A.M. Morega, L. Pîslaru-Dănescu, M. Morega, G. Telipan, "The design of the secondary electrical circuit of a flyback transformer with hybrid magnetic core", *Advanced Topics in Electrical Engineering*, ATEE 2019, Bucharest, Romania.
- [42] **Y. Veli**, A. M. Morega, M. Morega and L. Pîslaru-Dănescu, "Numerical modeling of a planar transformer for micro-power controllers," *10th International Symposium on Advanced Topics in Electrical Engineering (ATEE)*, Bucharest, 2017, pp. 206-210, doi: 10.1109/ATEE.2017.7905119.
- [43] **Y. Veli**, A.M. Morega, "Analiza prezentei unui ecran magnetic poziționat în spațiul dintre înfășurările unui transformator monofazat, de mică putere", Simpozionul de Mașini electrice, București, 2020.
- [44] I. Hernandez, F. De Leon, P. Gomez, „Design formulas for the leakage inductance of a toroidal distribution transformers”, *IEEE Transactions on Power Delivery*, **26**, 4, 2011.
- [45] S. Sudevalayam, P. Kulkarni, "Energy harvesting sensor nodes: survey and implications", 10.1109/SURV.2011.060710.00094, *IEEE Communications surveys & tutorials*, vol. 13 (3), THIRD QUARTE, 2011.
- [46] A.M. Morega, J. Ordondez, M. Morega, L. Pîslaru-Dănescu, A.A. Dobre, "Compact, interdigitated constructal design applied to supercapacitor systems", *PROCEEDINGS OF THE ROMANIAN ACADEMY, Series A, OF THE ROMANIAN ACADEMY, Special Issue/2018*, pp. 255–260.
- [47] H.M Ahmad Fahmy, "Concepts, applications, experimentation and analysis of wireless sensor networks", ediția 2, Springer, <https://doi.org/10.1007/978-3-030-58015-5>.
- [48] M.U.H. Al Rasyid, F.A. Saputra, MH. Ramdhani Ismar, "Performance of multi-hop networks using beacon and non-beacon scheduling in wireless sensor network (wsn)", *2015 International Electronics Symposium (IES)*.